ELSEVIER

Contents lists available at ScienceDirect

Geothermics

journal homepage: www.elsevier.com/locate/geothermics





Gas equilibrium in the H₂O-H₂-CO₂-CO-CH₄ system for wet-steam geothermal-well fluids and their sources: A case study from Krafla, Iceland

Giulio Bini ^{a,*}, Matteo Lelli ^{b,c}, Stefano Caliro ^d, Tullio Ricci ^e, Anette K. Mortensen ^f, Ásgerður K. Sigurðardóttir ^f, Alessandro Santi ^d, Antonio Costa ^a

- ^a Istituto Nazionale di Geofisica e Vulcanologia, Sezione di Bologna, viale Berti Pichat 6/2, 40127 Bologna, Italy
- b Institute of Geosciences and Earth Resources, National Research Council, Via G. Moruzzi 1, 56124 Pisa, Italy
- ^c Istituto Nazionale di Geofisica e Vulcanologia, Sezione di Pisa, via C. Battisti, 53, 56125 Pisa, Italy
- d Istituto Nazionale di Geofisica e Vulcanologia, Osservatorio Vesuviano, Sezione di Napoli, via Diocleziano 328, 80124 Napoli, Italy
- ^e Istituto Nazionale di Geofisica e Vulcanologia, Sezione Roma 1, via di Vigna Murata 605, 00143 Roma, Italy
- ^f Landsvirkjun, Háaleitisbraut 68, 103 Reykjavík, Iceland

ARTICLE INFO

Keywords: Geothermal resource monitoring Wet-steam well fluids Gas geothermometry Carbon monoxide N isotope fractionation

ABSTRACT

Equilibrium in the H₂O-H₂-CO₂-CO-CH₄ gas system has been extensively applied to fumarole data for geothermal exploration and volcano monitoring. However, little is known about its application to two-phase (vapor and liquid) geothermal well fluids, which can show an excess of enthalpy. Here, we applied the H2O-H2-CO2-CO-CH4 gas indicators to two-phase geothermal well discharges from the Krafla geothermal system, Iceland, to estimate aquifer temperatures and identify secondary processes during resource exploitation. Results suggest that the Krafla resource is drawn from a deep (approximately between -500 and -1,600 m a.s.l.), two-phase aquifer with temperatures ranging from 272 to 320 °C and vapor fractions between 0.26 and 0.93, explaining the excess enthalpy observed in well fluids. These estimates align with the temperatures of the main production zones of geothermal wells, whereas solute geothermometers (SiO2 and Na/K) appear to record lower temperatures of minor, shallower, liquid aquifers. Wells with liquid-like enthalpy are sourced from the two-phase aquifer but are also influenced by water reinjection or downflows from a colder, shallower aquifer, consistent with the isothermal zone extending approximately between 400 and -900 m a.s.l. in Leirbotnar and Vesturhlíðar subfields. Water isotopes indicate the main aquifer is recharged by meteoric and reinjection fluids. Excess-enthalpy discharges show an influx of Ar- and N_2 -rich vapor, with depleted 40 Ar/ 36 Ar and δ^{15} N values, suggesting fractionations of atmospheric gases dissolved into the reservoir liquid. On the other hand, $\delta^{13}C_{CO2}$ and ${}^{3}He/{}^{4}He$ values point to a mantle origin, despite the lower $\delta^{13}C_{CO2}$ and P_{CO2} levels that reflect a degassed magma (i.e., a noneruptive phase). These findings underscore the usefulness of the H2O-H2-CO2-CO-CH4 gas system and isotopic methods in tracking geothermal reservoir temperatures, their sources, and secondary processes, such as water reinjection or downflows from shallower aquifers.

1. Introduction

Geothermal energy harnesses the Earth's natural heat flow and is an important renewable resource to reduce the anthropogenic impact on climate. The natural heat flow can either be directly used for space heating, fish farming, and greenhouse heating, or exploited to produce electricity through high- and medium-enthalpy geothermal systems (Lund and Toth, 2021). High-enthalpy geothermal systems are generally developed in volcanic areas, where heat loss from shallow magmatic intrusions drives the convection of fluids circulating in the crust (Hayba and Ingebritsen, 1997). Depressurization causes steam separation,

which can be harnessed for electricity production through turbines (Truesdell and White, 1973). At the end of 2022, the worldwide geothermal installed capacity for electricity generation accounted for >16 GWe from 32 countries (Gutiérrez-Negrín, 2024).

The geothermal fluid is generally dominated by meteoric water and partly by magmatic fluids and its chemical composition is controlled by reactions with the minerals of the hosting rock, which are altered into hydrothermal (secondary) minerals, reaching equilibrium with the fluid (Giggenbach, 1980, 1981; Arnórsson et al., 2007; Cioni and Marini, 2020). These chemical reactions depend on temperature, pressure, activities of relevant solutes, and fugacities of gases. Hence, the analysis of

* Corresponding author.

E-mail address: giulio.bini@ingv.it (G. Bini).

https://doi.org/10.1016/j.geothermics.2025.103322

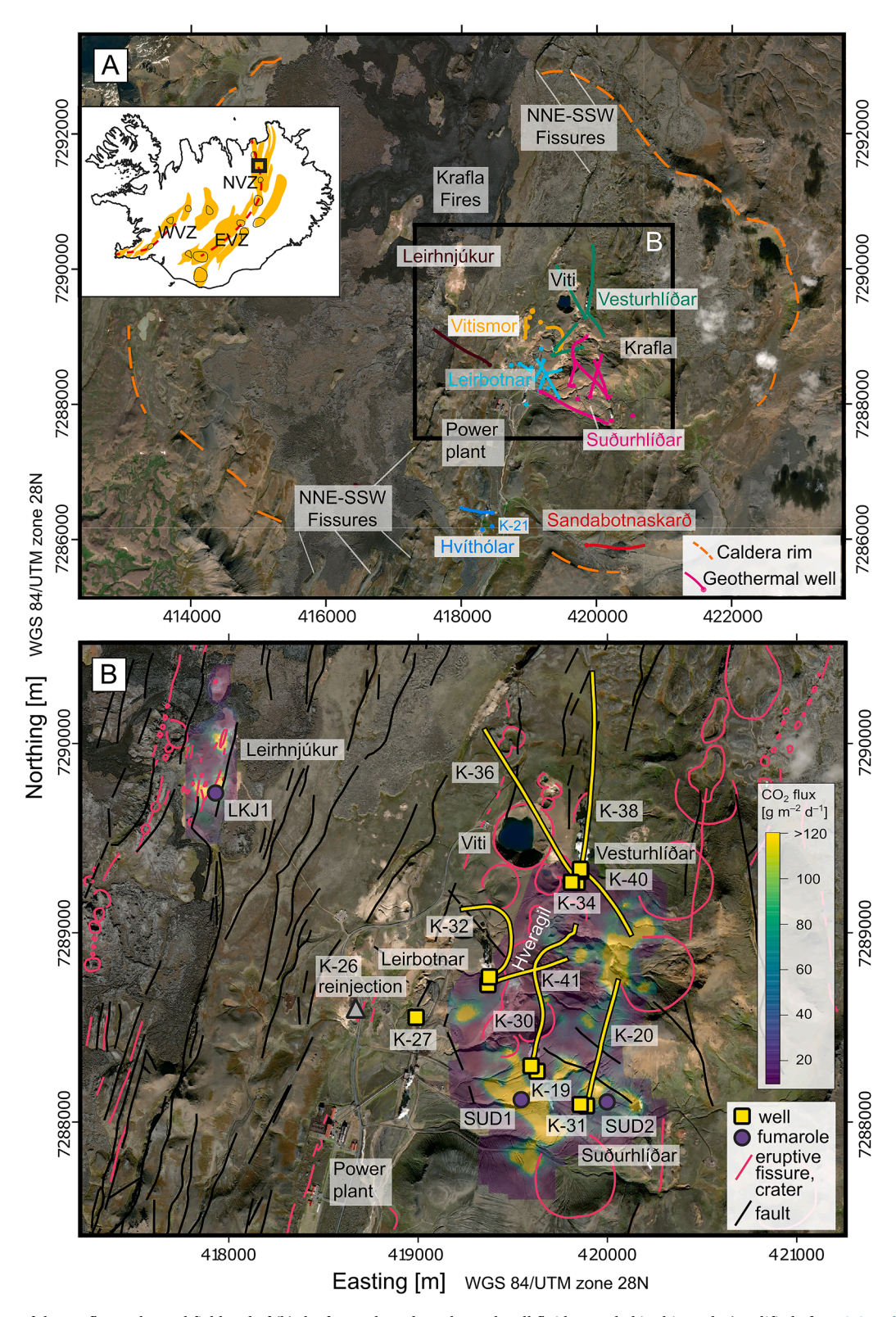


Fig. 1. (a) Location of the Krafla geothermal field and of (b) the fumarole and geothermal well fluids sampled in this study (modified after Bini et al. (2024)). (a) The geothermal field lies within the 8–10 km-width caldera of Krafla (orange line) in the Northern Volcanic Zone (NVZ) of Iceland (inset in panel a) and consists of 5 subfields: Leirbotnar (Vitismor included), Suðurhlíðar, Vesturhlíðar, Hvíthólar, and Sandabotnaskarð (Árnason, 2020; Scott et al., 2022). (b) Enlargement of the Krafla geothermal field shows the location of 12 of the 17 productive wet-steam wells sampled in 2022 (yellow square), together with three fumarolic vents (purple circle). The yellow squares depict the wellheads, whereas the yellow lines show the well tracks. Eruptive fissures and explosion craters (red line), and faults (black line; from Sæmundsson, 2008) are also shown. Maps of the soil CO_2 emission (g m⁻² d⁻¹) from the productive area of the geothermal field and Leirhnjúkur reveal that the hydrothermal fluid upflow is controlled by tectonics, following the normal faults parallel to the direction of the rift (NNE-SSW) and WNW-ESE faults (modified after Bini et al., 2024). The inset in (a) (modified after Árnason, 2020) also shows the location of the Western and Eastern Volcanic Zone (WVZ and EVZ), the fissure swarms (yellow areas), the main central volcanoes (black contours), and the spreading zones (red dashed lines) of Iceland. Background is from ESRI imagery.

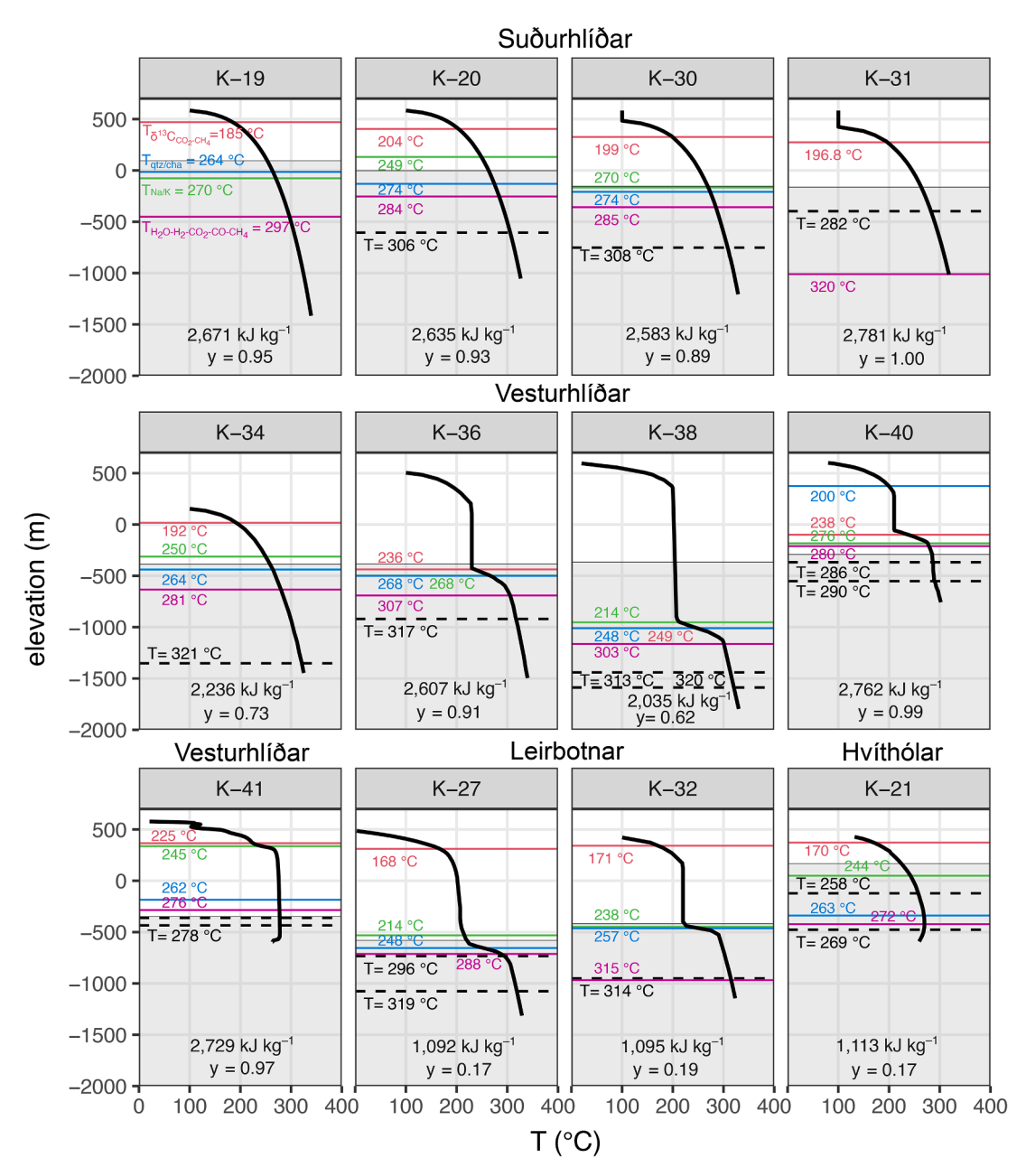


Fig. 2. Formation temperatures (black solid line) estimated after well completion (except K-41, which reports measured temperatures) and temperatures of the main productive feed zones (except that of K-19, which is unknown; black dashed line). The white area depicts the extent of the well casing, whereas the grey area indicates the section of the well below the casing, which is completed with the liner, that is, the zone from which fluids are extracted for geothermal production. The Suðurhlíðar subfield is characterized by boiling conditions along the entire length of the wells, whereas Leirbotnar also shows a shallow isothermal zone, reflecting a shallower liquid aquifer. Vesturhlíðar is characterized by both of these two conditions. The temperatures estimated with solute and gas geothermometers are plotted as horizontal solid lines, color coded for $\delta^{13}C_{CO2\text{-}CH4}$ (red), quartz/chalcedony (blue), Na/K (green), and H₂O-H₂-CO₂-CO-CH₄ (violet). The total discharge enthalpy of the wells (kJ kg⁻¹) and the fraction of vapor at the separator (y) are also shown.

the chemicals in the discharging fluids can shed light on such thermodynamics properties of the geothermal reservoir, assuming they do not re-equilibrate during the upflow from the aquifer to the surface. This assumption is usually fulfilled in geothermal well fluids, as the timescale of fluid upflow is negligible with respect to the residence time in the producing aquifers. However, this hypothesis may not be valid if the geothermal well produces from distinct feed zones with significantly different conditions. On the other hand, unreactive chemical species such as N_2 , He, Ar and their isotopes can track the sources of the fluids, as noble gases are inert and N_2 is negligibly affected by chemical reactions (Giggenbach, 1991), while the Earth's reservoirs (atmosphere, groundwater, crust, and mantle) are fingerprinted by distinct isotope

signatures (Ozima and Podosek, 2002). In addition to oxygen and hydrogen isotopes of water, N₂-He-Ar isotopes can help us to better quantify the contribution of magmatic fluids added to the predominant meteoric geothermal fluids. Therefore, analyzing both reactive and unreactive chemical species – or tracers and geoindicators, respectively (sensu Giggenbach, 1991) – and relevant isotopes enables us to better understand the anatomy of a geothermal system by characterizing the productive aquifers and their temperatures and evaluating which one or ones contribute the most to the geothermal production. Furthermore, monitoring these species and isotopes during the exploitation of the resource can track variations in the hierarchical structure of aquifers sustaining production and ultimately track inflows of acidic magmatic

fluids, which could compromise the power plant.

Both liquid and gas geoindicators are employed to estimate the temperature and pressure of the hydrothermal-system zones where relevant species presumably equilibrate, but solute geothermometry is far more widely used for this purpose. The silica geothermometer relies on the temperature dependency of SiO₂ concentration in pure water, in equilibrium with water vapor and a silica mineral, and is one of the most used geoindicators for geothermal well fluids (Fournier and Rowe, 1962; Arnórsson, 1970; Fournier, 1973; Fournier and Potter, 1982a,b; Arnórsson et al., 1983a). However, it can be affected by secondary processes, such as steam separation and amorphous silica precipitation, hence overestimating and underestimating the actual temperature of the productive aquifers, respectively. The Na-K geothermometer (Fournier, 1979; Arnórsson et al., 1983a; Giggenbach, 1988) is not affected by steam separation and is weakly influenced by dilution with colder water low in Na and K (Fournier, 1981), but there is no single universally best Na-K geothermometer (Bird and Norton, 1981; Fournier, 1991; Cioni and Marini, 2020). Even selecting the most suitable Na-K function, it cannot be applied to dry steam well discharges and may yield high uncertainty for excess-enthalpy discharges with minimal liquid fraction at the separator. Many gas geothermometers based on both gas-mineral equilibria, such as those involving CO₂, H₂S, and H₂ (Giggenbach, 1980; Arnórsson and Gunnlaugsson, 1985), and gas-gas reactions, such as the H₂-Ar geothermometer (Giggenbach, 1991; Sepulveda et al., 2007), those for the H₂O-H₂-CO₂-CH₄-NH₃-N₂ system (Giggenbach, 1980), and those for the H₂O-H₂-CO₂-CO-CH₄ system (Bertrami et al., 1985; Chiodini and Marini, 1998) have been proposed. The introduction of CO in gas geothermometry (Bertrami et al., 1985; Chiodini and Marini, 1998) was a big step forward, as it is a reactive gas, which efficiently equilibrates at reservoir conditions and keeps memory of these conditions during the fast upflow to the surface. Although this CO-based indicator has been widely applied to fumarole vapor compositions, little is known about its applications to geothermal well discharges.

Here, we apply the H₂O-H₂-CO₂-CO-CH₄ gas equilibria to two-phase geothermal well discharges, assuming they are fully representative of reservoir conditions (Bertrami et al., 1985; Chiodini et al., 1993), to reconstruct the main feed zones of a geothermal system and their thermodynamic properties, as well as to study the processes occurring in the subsurface. Furthermore, we report an extensive set of chemical and isotopic compositions of H2O, CO2, N2, He, and Ar to shed light on the sources of the geothermal fluid. To this end, we chose as a key study the Krafla geothermal system, where such an extensive set of analyses has not been reported for the same samples, and little is known about CO-based geothermometry. Gas equilibria in the H2O-H2-CO2-CO-CH4 system enabled us to estimate the temperatures and the physical state of the main aquifer, and the secondary processes occurring during the production. The reliability of the H₂O-H₂-CO₂-CO-CH₄ geoindicators in predicting fluid temperature is shown by comparison with the temperatures of the geothermal-well productive feed-zones and those inferred through solute geothermometry. Finally, H2O, CO2, N2, Ar, and He isotopes track the contributions of air-saturated water (ASW) and magmatic fluids to the geothermal resource, and suggest isotopic fractionation of ASW in the geothermal system.

2. Geological setting

The Krafla volcano, situated in northeast Iceland, spans approximately 20 km in diameter and is located along a 90-km-long NNE-SSW fissure swarm (Fig. 1a). Krafla, along with Kverkfjöll, Askja, Fremrinámar, and Theistareykir, constitutes the northern volcanic zone (NVZ), reflecting neovolcanic rifting activity (Einarsson, 2008; Hjartardóttir et al., 2016). Approximately 110–115 ka BP, an 8–10 km-wide caldera formed in Krafla during a mixed basalt-rhyolite event, known as the Halarauður eruption (Rooyakkers et al. 2020). While recent magmatic activity has been predominantly basaltic, historical eruptions have also produced rhyolites. The last significant basaltic fissure

eruptions, known as the Krafla Fires, occurred between 1975 and 1984 within the caldera near the Leirhnjúkur area (Einarsson, 1991; Fig. 1). Recent geothermal drilling, particularly in wells KJ-39 and IDDP-1, has encountered rhyolitic melts at shallow depths (~2 km), overlying a deeper mafic reservoir of the magmatic plumbing system (Elders et al., 2011; Mortensen et al., 2010). These rhyolites exhibit petrological similarities to those erupted in 1724 during the formation of the Viti maar, suggesting their presence throughout the center of the caldera (Montanaro et al., 2021; Rooyakkers et al., 2021).

The central part of the caldera, particularly near the latest basaltic products of the Krafla Fires in Leirhnjúkur, hosts an active geothermal system predominantly located on the western and southern flanks of Mount Krafla (Fig. 1). Since 1974, a total of 43 geothermal wells have been drilled in this area. Currently, 17 of these wells are operational, collectively generating 60 MWe through the utilization of two turbines. Permeability is higher in the upper kilometer of the caldera fillings, consisting of alternating hyaloclastite and lava flows, but decreases at greater depths where intrusive crystalline bodies occur (Scott et al., 2022). Permeability is mainly developed along fractures that follow the main tectonic directions of the fissure swarm (NNE-SSW) and the WNW-ESE alignment, which has guided the drilling of recent geothermal wells (e.g., K-40, K-41; Fig. 1b; Mortensen et al., 2015).

The geothermal system can be segmented into five subfields based on the relationship between fractures, meteoric recharge flow, and the stratigraphy of the Krafla caldera (Fig. 1; Árnason, 2020; Scott et al., 2022). Leirbotnar (including Vitismor), situated west of the Hveragil fissure, features an isothermal zone at 190-220 °C extending to a depth of 1-1.5 km and a deeper boiling reservoir with temperatures exceeding 300 °C (Fig. 2). This isothermal zone is limited by an underlying low-permeability aquitard present at the lithological interface between the caldera fillings and intrusive bodies, coupled with the cooling influence of N-S flowing meteoric water (Stefánsson, 1981; Darling and Ármannsson, 1989; Pope et al., 2016; Scott et al., 2022). The Suðurhlíðar subfield exhibits boiling conditions from the surface to approximately 2-2.5 km depth, where temperature exceeds 300 °C (Fig. 2), indicating a principal upflow zone of fluids unobstructed by the aquitard, which terminates beyond the Hveragil fracture (Pope et al., 2016; Scott et al., 2022; Fig. 2). Vesturhlíðar, on the western flank of Mount Krafla and east of the Hveragil fissure (Fig. 1), shows boiling conditions at any depth in some wells, such as K-34, and a shallow sub-boiling zone in other wells, such as K-36, K-38, and K-40 (Fig. 2; Gudmundsson and Mortensen, 2015; Mortensen et al., 2015). Hvíthólar, situated in the southern part of the field (Fig. 1), appears to represent the peripheral zone of the main fluid upflow focused in the previous subfields, as suggested by the temperature inversion at approximately 500 m b.s.l., such as in well K-21 (Scott et al., 2022). Sandabotnaskarð is situated south of Suðurhlíðar and east of Hvíthólar (Fig. 1). Despite the diverse thermal conditions of these subfields at depths of <1.5 km, the primary production area consistently exhibits boiling zones and superheated/supercritical conditions at greater depths (Fig. 2), as observed in wells KG-04, KG-25, KJ-36, KJ-39, and IDDP-1 (Mortensen et al., 2015).

Soil CO_2 emission has been recently measured in both the main production area of the geothermal field (Suðurhlíðar, Vesturhlíðar, and part of Leirbotnar) and Leirhnjúkur, revealing that the degassing is controlled by tectonics, along normal faults with the same NNE-SSW direction of the rift and WNW-ESE fractures (Fig. 1b; Bini et al., 2024). The natural amount of CO_2 released into the atmosphere accounted for $62.5 \text{ t} \text{ d}^{-1}$ and $7.1 \text{ t} \text{ d}^{-1}$ from the main production area and Leirhnjúkur, respectively (Bini et al., 2024). Soil CO_2 emission spatially correlates with the temperature at 15 cm depth in Leirhnjúkur and Suðurhlíðar, reflecting boiling and condensation of the vapor upflow from the geothermal system, consistent with the natural state temperature-depth profiles (Fig. 2). The lower temperature and weak spatial correlation with CO_2 fluxes in Vesturhlíðar is instead explained by the presence of a liquid aquifer at shallower depth (Fig. 2; Bini et al., 2024). In the root of the geothermal system, supercritical fluids with a

thermal power in the order of 800 MW in Suðurhlíðar — up to 1.5 GW in the main production area — formed near shallow magmatic intrusions and could sustain the geothermal fluid flow and the emission of $\rm CO_2$ from soils (Bini et al., 2024).

The chemical and isotopic compositions of the Krafla geothermal fluids have been investigated for various purposes, such as geothermal production (Gudmnundsson and Arnórsson, 2002) and volcano monitoring (Ármannsson et al., 1989) during the Krafla Fires (1975–1984), as well as for studying supercritical fluids forming around shallow magmatic intrusions (Stefánsson, 2014; Heřmanská et al., 2019). Water isotope systematics (δD_{H2O} and $\delta^{18}O_{H2O})$ indicate that hydrothermal fluids at Krafla and other NVZ volcanoes (Kverkfjöll, Askja, Namafjall, and Theistareykir) originate from meteoric water (Pope et al., 2016; Stefansson et al., 2017; Ranta et al., 2023). Argon isotopes also indicate a predominantly atmospheric source in both Krafla (40 Ar/ 36 Ar of 303.2 and 304.9 in well K-8 and K-15, respectively; Sano et al., 1985) and Theistareykir fluids (40 Ar/36 Ar spanning the 284.4–307.3 range; Saby et al., 2020). Few studies reported N isotopes of Icelandic geothermal fluids (Sano et al., 1985; Ármannsson et al., 1989; Marty et al., 1991; Óskarsson et al., 2015; Labidi et al., 2020). Among them, only Sano et al. (1985) and Ármannsson et al. (1989) analyzed $\delta^{15}N$ in four Krafla well discharges (K-7, K-8, K-15, and K-22), reporting positive values (from 0.2 to 4 % vs. atmosphere). Carbon dioxide in Krafla fluids is primarily mantle derived (Barry et al., 2014; Stefansson et al., 2017), as are helium isotopes (Furi et al., 2010). Within the NVZ, both geothermal fluids and volcanic glasses show an increase in ³He/⁴He ratios towards the north (8.4–11.5 Ra¹; Furi et al., 2010; Harðardóttir et al., 2018; Saby et al., 2020; Ranta et al., 2023). Higher ³He/⁴He ratios are also observed south of the NVZ (16.7-19.2 Ra; Furi et al., 2010) and in the WVZ (9.7-17.4 Ra; inset in Fig. 1a; Furi et al., 2010). The highest plume-like values (>20 Ra), indicative of a deep mantle contribution, are found far from the neovolcanic zone in the South Iceland Seismic Zone (SISZ), a transform fault system separating the EVZ and the WVZ, as well as in Vestfirðir (NW Iceland; Furi et al., 2010).

3. Methods

3.1. Sampling of fumarole vapors and wet-steam well fluids

Vapor and liquid phases were collected from 3 fumarolic vents and 12 two-phase geothermal well discharges at Krafla in August 2023 (Fig. 1). Up to four gas samples were collected from each fumarolic vent located in Leirhnjúkur (LKJ1) and the Suðurhlíðar geothermal subfield (SUD1, SUD2). The sampling was carried out through a 1-meter-long titanium tube inserted into the vent or a funnel positioned upside down over the steam emission, connected to a Pyrex glass pipe. For the first gas sample, a 140 mL evacuated Pyrex glass flask containing 50 mL of a 4 N NaOH solution was used, as described by Giggenbach (1975) and Giggenbach and Goguel (1989). Water vapor and reactive gases, such as CO₂ and H₂S, were absorbed in the alkaline solution, whereas non-reactive gases (N2, O2, CO, H2, He, Ar, and CH4) remained in the flask headspace. The second, third, and fourth gas samples were collected simultaneously by pumping the gas through a water-cooled condenser attached to the sampling line (Cioni and Corazza, 1981). The condensed vapor phase (second gas sample) was stored in a 50 mL high-density polyethylene bottle, whereas the dry gas phase was collected in two separate 20 mL Pyrex glass flasks with two Teflon stopcocks at both ends (third and fourth gas samples). The fourth gas sample was not collected from fumarole SUD2. To prevent air contamination during sampling, precautions such as a submerged exhaust after the glass flask, sealing of the sampling line junctions with gaskets or high-vacuum grease, and slow gas pumping were implemented.

Vapor and liquid samples from geothermal well discharges were collected through a mini Webre separator connected to the two-phase pipeline close to the wellhead. For the vapor phase, up to four gas samples were collected with the same methodology used for fumarole vapors. The fourth gas sample was not collected for wells K-27, K-34, and K-40. For the liquid phase, we collected samples after circulating the separated liquid in a stainless-steel coil submerged in cold water to reduce its temperature. Details on sampling and chemical analyses of liquid phases are reported in the Supplementary Material.

3.2. Chemical and isotopic analysis of fumarole vapors and two-phase geothermal well fluids

The collected samples were analyzed for chemical and isotopic compositions at the Laboratory of Fluid Geochemistry of the Istituto Nazionale di Geofisica e Vulcanologia, Sezione di Napoli, Osservatorio Vesuviano (INGV-OV), Italy, following the protocols described in Caliro et al. (2015) and afterwards improved. The gas mixture in the headspace of the first gas sample was analyzed for He, H2, Ar, O2, N2, and CH4, nitrogen isotopes $(\delta^{15}N = [(^{14}N^{15}N/^{14}N^{14}N)_{sample}/(^{14}N^{15}N/^{14}N^{14}N)]$ $N^{14}N)_{atmosphere} - 1$] x 1000), argon isotopes (⁴⁰Ar and ³⁶Ar), and C isotopes of methane ($\delta^{13}C_{CH4}$ in ‰ vs. V-PDB) using an instrumental setup specially developed and dedicated to these type of analyses. This instrumental setup consists of a continuous flow mass spectrometer (MS, Thermo Fischer Delta V) equipped with ten collectors for simultaneous determination of the relative abundance of the masses 36, 38, 40 and 28, 29, 30 and, using a peak jump procedure in the same run, also the masses 44, 45, and 46. The gas in the headspace of the vials was injected into a gas chromatograph (Thermo Trace 1310) with two channels equipped with six-port injection valves, PLOT columns (molecular sieves, 5 Å; 30 $m\times 0.53~mm\times 50~\mu m),$ and thermal conductivity detectors. The first channel analyzed He and H2 using Ar as a carrier gas. The second channel, with He as a carrier gas and a post-column switching device, splits the column gas flow to the TCD for chemical analyses and to the MS for the determination of the isotopic compositions of 40 Ar/ 36 Ar, δ^{15} N (analytical error of \pm 0.1 %) and $\delta^{13}C_{CH4}$ (analytical error of \pm 0.2 %) on the same gas aliquot. To analyze the $\delta^{13}C_{CH4}$, the gas after the post-column split passes through an oxidizing oven held at 1000 °C (GC Isolink) to convert the methane to CO2 and analyze it for 44, 45, and 46 masses on the MS. This determination of $\delta^{13}C_{CH4}$ (as CO_2) value is made possible in the same run using a fast peak jump procedure, which allows a rapid change of the MS magnetic configuration, taking into account the magnet hysteresis. The NaOH solution in the first gas sample was oxidized with H₂O₂ to convert absorbed H₂S into SO₄² for ion chromatography analysis (Dionex ICS-3000). The CO2 concentration was determined by acidimetric titration of CO_3^{2-} (analytical error \pm 3 %) in the NaOH solution.

The second gas sample (steam condensate) was analyzed for hydrogen and oxygen isotopes of H_2O (δD_{H2O} and $\delta^{18}O_{H2O}$ in ‰ vs. V-SMOW) using a near-infrared laser analyzer (Picarro L2130-i; analytical error of \pm 0.5 % on δ_D and \pm 0.08 % on δ^{18} O). The third gas sample (dry gas) was analyzed for CO using a gas chromatograph equipped with a high-sensitivity reducing compound photometer (Peak Performer 1 RCP, Peak Laboratories; detection limit 0.001 ppm). The gas mixture in the headspace of the first gas sample is not suitable for CO determination due to its partial conversion in COOH ion in the alkaline solution (Giggenbach and Matsuo, 1991). Additionally, carbon and oxygen isotopes of CO₂ (δ^{13} C_{CO2} in % vs. V-PDB and δ^{18} O_{CO2} in % vs. V-SMOW) were analyzed in the third gas sample by mass spectrometry after gas chromatographic separation using the GasBench II device (analytical error of \pm 0.08 % on δ^{18} O and \pm 0.06 % on δ^{13} C). Helium isotope analysis was performed on the fourth gas sample (dry gas) at the Laboratory of the Istituto Nazionale di Geofisica e Vulcanologia, Sezione di Palermo (INGV-PA), Italy. The isotopic composition of He (³He/⁴He) and ²⁰Ne in the flask were measured by introducing He and Ne separately into a split flight tube mass spectrometer (GVI-Helix SFT for He)

 $^{^1}$ Ra is the $^3\text{He}/^4\text{He}$ ratio in air, which is usually assumed to be $1.39\times10^{-6},$ in spite of some doubts (Mishima et al., 2018).

and into a multicollector mass spectrometer (Thermo-Helix MC plus for Ne), following standard purification procedures (see Rizzo et al., 2016).

3.3. Composition of the total gas discharge from geothermal wells

The chemical composition of geothermal well fluids is expressed as total discharge, whereas fumarole vapor composition does not require further calculation. The fraction of vapor in wet-steam well discharges, that is, discharges of liquid and vapor mixtures, is calculated through the total enthalpy of the fluid and the separation pressure in the mini Webre separator according to

$$y = \frac{h_d - h_l}{h_v - h_l} \tag{1}$$

where y is the mass fraction of vapor, h_d is the total discharge enthalpy (kJ kg $^{-1}$), and h_l and h_v are the enthalpies (kJ kg $^{-1}$) of the saturated liquid and vapor, respectively, at the separation pressure-temperature. Most of the geothermal well fluids of Krafla show excess-enthalpy, namely the h_d is higher than the enthalpy of saturated liquid water at the aquifer temperature. The y is then used to calculate the total discharge composition according to

$$C_{i,d} = C_{i,\nu} \times y + \frac{C_{i,\nu}}{R_i} \times (1 - y)$$
(2)

where $C_{i,d}$ and $C_{i,\nu}$ are the concentrations of the gas species i (mg kg⁻¹) in the total discharge and in the separated vapor phase, respectively, and B_i is its vapor-liquid distribution coefficient ($C_{i,\nu}/C_{i,l}$). The dependency of the log B on temperature (t in °C) in the range 100–340 °C for each gas species analyzed in this study (CO₂, H₂S, Ar, N₂, CH₄, H₂, He, and CO) is reported in Table S1.

3.4. Gas equilibria in the H2O-H2-CO2-CO-CH4 system

Gas equilibrium among H2O, H2, CO2, CO, and CH4 in fumaroles and geothermal well fluids was studied using two theoretical reference models. Model 1 (Chiodini and Marini, 1998) assumes the presence of a single liquid phase in the geothermal aquifer, adiabatic boiling of the liquid, and vapor separation in a single-step. Model 2 (Bertrami et al., 1985; Chiodini et al., 1993) is based on the equations of Giggenbach (1980), which enable the presence of a liquid phase coexisting with an equilibrium vapor phase in the geothermal aquifer. The surface discharge is assumed to be a mixture of aquifer liquid and equilibrium vapor or a fluid remaining after the removal of a given fraction of equilibrium vapor from the original aquifer liquid. In other words, the second approach allows us to model the effects of loss or gain of vapor with respect to the composition and enthalpy expected for the discharge of a pure equilibrium liquid. Geothermal well fluids with liquid-enthalpy at reservoir condition can be reproduced with both models setting the equilibrium vapor fraction to zero. Fumarole gases can be studied with model 1, whereas model 2 is suitable to investigate wet-steam well discharges with excess-enthalpy. The excess enthalpy can be either a natural condition due to the presence of vapor coexisting with the liquid in the geothermal aquifer or developed upon production. Whether or not a vapor phase naturally coexisted with the liquid in the Krafla geothermal aquifer before its exploitation, it is reasonable to expect that steam zones have developed in the geothermal aquifers after 50 years of production (since 1974). For example, conductive heat

transfer from the host rock to the cooling geothermal fluids due to depressurization boiling or segregation of the liquid phase in the rock pores may contribute to increase the vapor fraction in the well discharge (Glover et al., 1981; Arnórsson et al., 2007). These processes have been investigated through different approaches, which need some peculiar parameters to be fixed, such as the aquifer and the phase segregation temperatures or the vapor fraction assuming either homogeneous equilibrium between CH₄, H₂O, H₂, and CO₂ or heterogeneous (gasmineral) equilibrium between H₂, H₂S, pyrite and magnetite, or both of them (Arnórsson et al., 2007; Scott et al., 2014). Since the heterogeneous equilibrium hypothesis is equivalent to fixing redox conditions, which are unknown and depend on the chosen minerals, we prefer to assume the attainment of homogeneous equilibrium between gas species and to work with both redox-dependent and redox-independent reactions in both models 1 and 2.

Model 1 – As shown by Chiodini and Marini (1998) and Marini et al. (2022) the equilibrium among H_2O , H_2 , CO_2 , and CO can be described by two redox-dependent reactions

$$H_2O = H_2 + \frac{1}{2}O_2 \tag{3}$$

and

$$CO_2 = CO + \frac{1}{2}O_2 \tag{4}$$

whereas in the $H_2O-H_2-CO_2-CO-CH_4$ gas system, the equilibrium condition can be attained by five redox-independent reactions (Chiodini and Marini, 1998), among which we consider the

$$CO_2 + H_2 = CO + H_2O (5)$$

$$3CO_2 + CH_4 = 4CO + 2H_2O (6)$$

and

$$CO_2 + 4H_2 = CH_4 + 2H_2O (7)$$

which are named reverse water-gas shift (RWG), CCC reaction, and Sabatier-Senderens reduction (SS4), respectively. Assuming ideal gas behavior and rearranging the logarithms of the thermodynamic equilibrium constants of the five reactions 3–7 (K_{H2} , K_{CO} , K_{RWG} , and K_{CCC} , K_{SS4}), we can express the temperature dependence of log-ratios of gas mole fractions or sums of log-ratios of gas mole fractions. For the redox-dependent reactions 3 and 4, the considered log-ratios of gas mole fractions are

$$log\left(\frac{X_{H_2,\nu}}{X_{H_2,0,\nu}}\right)_{t_S} = logK_{H_2} - \frac{1}{2}logf_{O_2} - log\left(s + \frac{(1-s)}{B_{H_2,t_S}}\right) - logB_{H_2,t_O}$$
(8)

and

$$log\left(\frac{X_{CO,\nu}}{X_{CO_{2},\nu}}\right)_{t_{S}} = logK_{CO} - \frac{1}{2}logf_{O_{2}} - log\left(s + \frac{(1-s)}{B_{CO,t_{S}}}\right) + log\left(s + \frac{(1-s)}{B_{CO_{2},t_{S}}}\right) - log\left(\frac{B_{CO,t_{O}}}{B_{CO_{2},t_{O}}}\right)$$
(9)

For the redox-independent reactions 5, 6, and 7 the considered sums of log-ratios of gas mole fractions are

$$log\left(\frac{X_{H_{2,O,V}}}{X_{H_{2,V}}}\right)_{t_{S}} + log\left(\frac{X_{CO,V}}{X_{CO_{2,V}}}\right)_{t_{S}} = logK_{RWG} - log\left(s + \frac{(1-s)}{B_{CO,t_{S}}}\right) - logB_{CO,t_{O}} + log\left(s + \frac{(1-s)}{B_{CO_{2},t_{S}}}\right) + logB_{CO_{2},t_{O}} + log\left(s + \frac{(1-s)}{B_{H_{2},t_{O}}}\right) + logB_{H_{2},t_{O}}$$

$$(10)$$

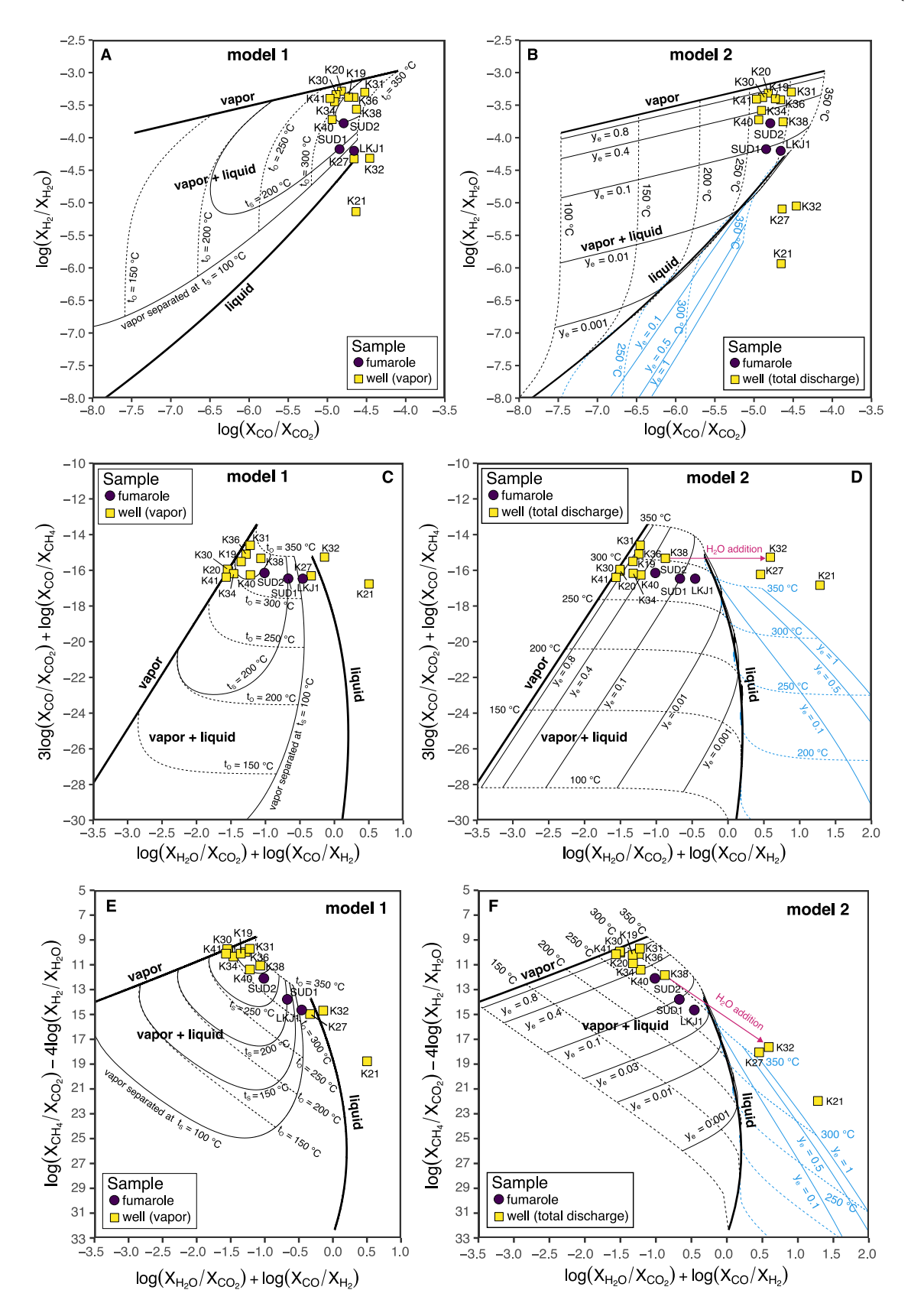


Fig. 3. Theoretical grids in the (a, b) $\log(X_{H2}/X_{H2O})$ vs. $\log(X_{CO}/X_{CO2})$ space, (c, d) $3\log(X_{CO}/X_{CO2}) + \log(X_{CO}/X_{CH4})$ vs. $\log(X_{H2O}/X_{CO2}) + \log(X_{CO}/X_{H2})$ space, and (e, f) $\log(X_{CH4}/X_{CO2}) - 4\log(X_{H2O}/X_{CO2})$ vs. $\log(X_{H2O}/X_{CO2}) + \log(X_{CO}/X_{H2})$ space describing (a, c, e) adiabatic boiling of liquids and single-step separation of vapor (model 1) and (b, d, f) coexistence of an equilibrium vapor and liquid phase in the reservoir (model 2). (a, b) Grids were constructed using the redox buffer of D'Amore and Panichi (1980), whereas (c, d, e, f) grids are independent from the redox potential. The blue grid (b, d, f) reflects liquids that have lost vapor through boiling. The red-pink arrow (d, f) shows that the addition of a 0.97 fraction of pure H₂O to the K-38 well fluids might explain the K-32 sample.

$$3log\left(\frac{X_{CO,\nu}}{X_{CO_{2},\nu}}\right)_{t_{S}} + log\left(\frac{X_{CO,\nu}}{X_{CH_{4},\nu}}\right)_{t_{S}} = logK_{CCC} - 2logP_{H_{2}O} - 4log\left(s + \frac{(1-s)}{B_{CO,t_{S}}}\right) - 4logB_{CO,t_{O}} + 3log\left(s + \frac{(1-s)}{B_{CO_{2},t_{O}}}\right) + 3logB_{CO_{2},t_{O}} + log\left(s + \frac{(1-s)}{B_{CH_{4},t_{O}}}\right) + logB_{CH_{4},t_{O}}$$

$$(11)$$

and and

$$log\left(\frac{X_{CH_4,\nu}}{X_{CO_2,\nu}}\right)_{t_S} - 4log\left(\frac{X_{H_2,\nu}}{X_{H_2O,\nu}}\right)_{t_S} = logK_{SS4} + 2logP_{H_2O} + 4log\left(s + \frac{(1-s)}{B_{H_2,t_S}}\right) + 4logB_{H_2,t_O}$$

$$-log\left(s + \frac{(1-s)}{B_{CH_4,t_S}}\right) - logB_{CH_4,t_O} + log\left(s + \frac{(1-s)}{B_{CO_2,t_S}}\right) + logB_{CO_2,t_O}$$
(12)

In Eqs. (8)–(12), $X_{i,v}$ is the mole fraction of the gas species i in the vapor phase, t_S is the temperature of vapor separation (t in °C), t_O is the original temperature of the liquid, f_{O2} is the redox potential, which can be fixed by empirical relationships such as that of D'Amore and Panichi (1980) — $\log f_{O2} = 8.20 - 23,643$ /T(K) — and s is the fraction of vapor separated calculated assuming enthalpy conservation through the following equation

$$s = \frac{h_{l,t_0} - h_{l,t_S}}{h_{v,t_S} - h_{l,t_S}} \tag{13}$$

The temperature dependence of the thermodynamic equilibrium constants (from Chiodini and Marini, 1998 and Marini et al., 2022) are reported in Table S1, whereas at saturation conditions (coexistence of liquid and vapor), the partial pressure of water (in bar) can be approximated by log $P_{\rm H2O}=5.51-2040/T(K)$ (Giggenbach, 1980).

Model 2 – The equations used to model geothermal well discharges fed by aquifer fluids consisting of equilibrium vapor and liquid are

$$\log\left(\frac{X_{H_2,d}}{X_{H_2,O,d}}\right) = \log K_{H_2} - \frac{1}{2}\log f_{O_2} - \log B_{H_2} + \log D_{H_2}^{\pm 1}$$
(14)

and

$$log\left(\frac{X_{CO,d}}{X_{CO_2,d}}\right) = logK_{CO} - \frac{1}{2}logf_{O_2} - log\left(\frac{B_{CO}}{B_{CO_2}}\right) + log\left(\frac{D_{CO}^{\pm 1}}{D_{CO_2}^{\pm 1}}\right)$$
(15)

for the redox-dependent reactions 3 and 4, and

$$\log\left(\frac{X_{H_2,0,d}}{X_{H_2,d}}\right) + \log\left(\frac{X_{CO,d}}{X_{CO_2,d}}\right) = \log K_{RWG} - \log\left(\frac{B_{CO}}{B_{CO_2}}\right) + \log B_{H_2} + \log\left(\frac{D_{CO}^{\pm 1}}{D_{CO_2}^{\pm 1}}\right) - \log D_{H_2}^{\pm 1} \tag{16}$$

$$log\left(\frac{X_{CH_4,d}}{X_{CO_2,d}}\right) - 4log\left(\frac{X_{H_2,d}}{X_{H_2O,d}}\right) = logK_{SS4} + 2logP_{H_2O} + 4logB_{H_2} - log\left(\frac{B_{CH_4}}{B_{CO_2}}\right)$$
$$-4logD_{H_2}^{\pm 1} + log\left(\frac{D_{CH_4}^{\pm 1}}{D_{CO_2}^{\pm 1}}\right)$$
(18)

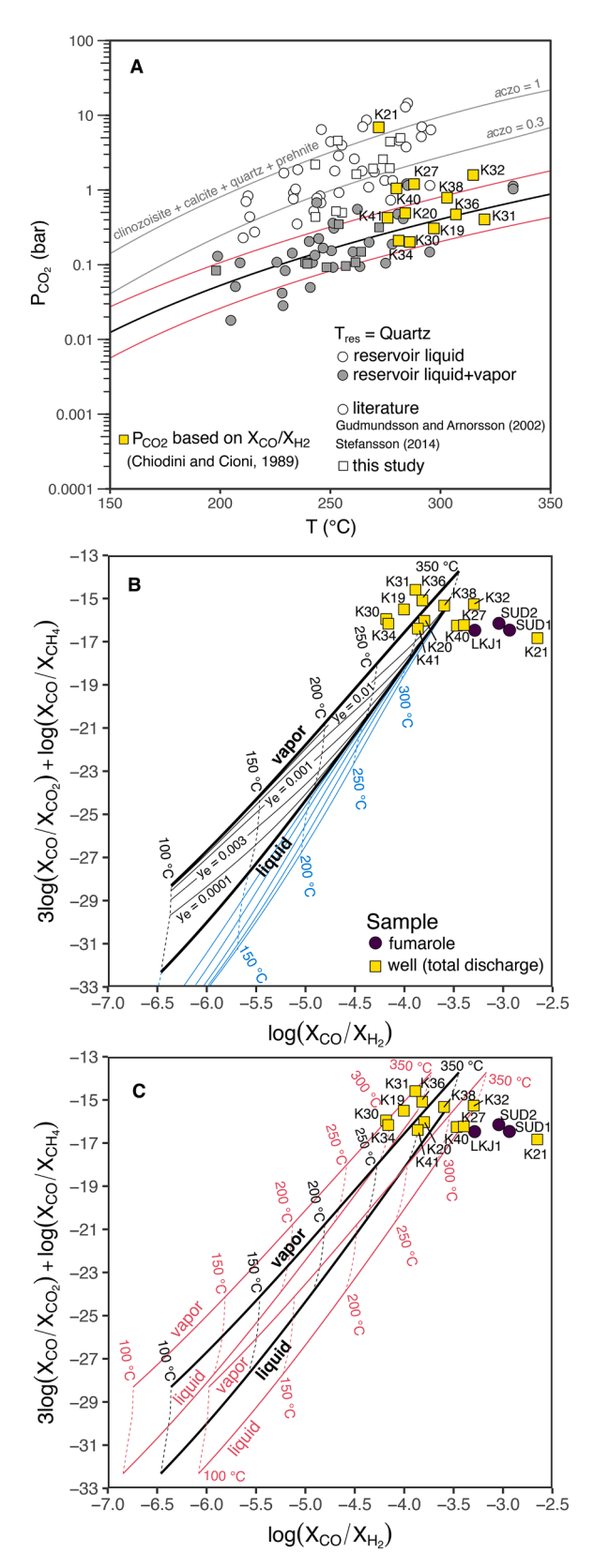
for the redox-independent reactions 5–7, where $X_{i,d}$ is the molar fraction of the gas species i in the total discharge and

$$D_i^{\pm 1} = 1 - y_e + y_e \times B_i \tag{19}$$

where y_e is the fraction of equilibrium vapor (Giggenbach, 1980). The positive sign refers to addition of equilibrium vapor to a reservoir liquid (i.e., equilibrium coexistence of steam and liquid in the geothermal aquifer), whereas the negative sign refers to loss of equilibrium vapor from the reservoir liquid, namely a boiled liquid that has lost part of the gas species i, including H_2O . For $y_e=1$, Eqs. (14)–(18) describe equilibrium in a single vapor phase, whereas for $y_e=0$ they describe equilibrium in a single liquid phase. The equilibrium temperature of vapors separated adiabatically in a single step from boiling liquids (Eq. (8)–(12)) and the equilibrium vapor fraction and temperature of wet-steam well discharges (Eq. (14)–(18)) were evaluated by comparing the analyzed fumarole vapor and total well discharge compositions by means of theoretical grids (Figs. 3, 4b). More accurate results were obtained by solving the equations by iterations until convergence was achieved.

These geothermometers based on the H₂O-H₂-CO₂-CO-CH₄ gas system (Chiodini and Marini, 1998) assume equilibrium among these species and rely on the same fundamental hypotheses as all water- and gas-geothermometers. These principles (Fournier et al., 1974), include that (i) temperature-dependent reactions occur at depth; (ii) all components involved in a temperature-dependent reaction are sufficiently abundant, that is their availability is not a limiting factor; (iii) fluid-rock

$$3log\left(\frac{X_{CO,d}}{X_{CO_2,d}}\right) + log\left(\frac{X_{CO,d}}{X_{CH_4,d}}\right) = logK_{CCC} - 2logP_{H_2O} - 3log\left(\frac{B_{CO}}{B_{CO_2}}\right) - log\left(\frac{B_{CO}}{B_{CH_4}}\right) + 3log\left(\frac{D_{CO}^{\pm 1}}{D_{CH_4}^{\pm 1}}\right) + log\left(\frac{D_{CO}^{\pm 1}}{D_{CH_4}^{\pm 1}}\right)$$
(17)



(caption on next column)

Fig. 4. (a) Partial pressure of CO_2 (P_{CO2}) with temperature and (b, c) theoretical grids in the $3log(X_{CO}/X_{CO2})$ + $log(X_{CO}/X_{CH4})$ vs. $log(X_{CO}/X_{H2})$ space describing the coexistence of an equilibrium vapor and liquid phase in the reservoir. (a) White symbols refer to P_{CO2} and temperatures of our samples and literature well-fluid data (Gudmundsson and Arnórsson, 2002; Stefánsson, 2014) modeled through WATCH (Bjarnason, 2010) using quartz temperature (Fournier and Potter, 1982b) and assuming a liquid reservoir, whereas grey symbols refer to the same computation assuming a vapor-liquid reservoir. The clinozoisite-calcite-quartz-phrenite mineral buffer (Table S2; grey curve) with variable activity of clinozoisite (from 0.3 to 1) and the P_{CO2} -temperature relationship found by fitting the grey samples (Eq. 25; black solid line) are also reported. The red curves reflect the 63.8 % prediction band of this latter fit, that is, an uncertainty equals to one standard deviation. The yellow squares depict the temperatures estimated with the H2O-H2-CO2-CO-CH4 gas system for wet-steam wells (Section 3.4) and the PCO2 based on the XCO/XH2 ratio (Chiodini and Cioni, 1989; Table S2). (b, c) Theoretical grids of vapor-liquid coexistence are constructed using the P_{CO2} -temperature dependence of Eq. (25) (black grid in b, c) and its uncertainty (red grids in c).

equilibration occurs at the reservoir temperature; (iv) the fluid maintains its composition with little to no re-equilibration or alteration at lower temperatures during its ascent from the reservoir to the surface; (v) the fluid originating at depth in the system does not mix with cooler, shallower fluids.

The original functions of Chiodini and Marini (1998) for the system $\rm H_2O\text{-}H_2\text{-}CO_2\text{-}CO\text{-}CH_4}$ are not applicable to supercritical conditions, where temperature and pressure exceed the critical point of pure water (373.946 °C and 220.640 bar; Wagner and Pruss 2002). The limit of applicability was extended by Chiodini et al. (2001) to systems at temperatures up to approximately 500 °C by considering the binary $\rm H_2O\text{-}NaCl$ system and deriving solubility functions for NaCl brines up to 3 m, whereas possible deviations from the ideal gas behavior were not taken into account. Nevertheless, these limitations do not affect the Krafla geothermal fluids considered in this study, as the measured temperatures and pressures remain below the critical point of pure water.

3.4.1. Gas equilibria in the $H_2O_{(1)}$ - H_2 - CO_2 -CO- CH_4 system and P_{CO2} functions

Water vapor is the dominant species in fumarole and geothermal fluids (\sim 99 % molar) and hence, secondary processes, such as condensation or addition of steam, may cause large variation in the analyzed $X_{\rm H2O}/X_{\rm H2}$ ratio (Eqs. (8), (10), (12), (14), (16), and (18)). To avoid these effects, we considered the dry gas phase of geothermal fluids, by considering liquid water instead of water vapor in the RWG reaction, which is rewritten as

$$CO_2 + H_2 = CO + H_2O_{(l)}$$
 (20)

Assuming fugacity coefficients close to unity at the relatively high temperatures and low pressures of geothermal systems (<100 bar; Giggenbach, 1980), the equilibrium constant of the RWG reaction with liquid water (RWG,l) can be expressed as

$$K_{RWG,l} = \frac{P_{CO} \times a_{H_2O}}{P_{CO_2} \times P_{H_2}} \tag{21}$$

where P_i is the partial pressure of the species i and $a_{\rm H2O}$ is the activity of water, which is equal to one for pure water and close to one for low-salinity liquids. By substituting $P_i = X_{i,v} \times P_{tot}$ and using the decimal logarithms, we obtain

$$K_{RWG,l} = \frac{X_{CO,v} \times P_{tot}}{X_{H_2,v} \times P_{tot} \times P_{CO_2}}$$
(22)

and

$$log\left(\frac{X_{CO,\nu}}{X_{H_2,\nu}}\right) = logK_{RWG,l} + logP_{CO_2}$$
(23)

Table 1 Chemical composition (μ mol mol⁻¹) and oxygen and hydrogen isotopes of water (% vs. V-SMOW) of the total discharge from the wet-steam wells of Krafla (see Section 3.3). The mass flow (\dot{m}) and total discharge enthalpy (h_d) are also reported. C isotopes of CO₂ and CH₄ (% vs. V-PDB) and N (% vs. Atmosphere), Ar, and He isotopes refer to the analysis of the vapors collected at the mini Webre separator. The error for ⁴⁰Ar/³⁶Ar ratios is ±

Sample	Date	<i>ṁ</i> (kg s ⁻¹)	h _d (kJ kg ⁻¹)	H_2O	CO_2	H ₂ S	Ar	N_2	CH ₄	H ₂	Не	CO	$\delta^{18}O_{H2O}$	$\delta D_{\rm H2O}$	$\delta^{13}C_{CO2}$	$\delta^{13}C_{CH4}$	$\delta^{15} N$	⁴⁰ Ar/ ³⁶ Ar	³ He/ ⁴ He (R/Ra ^a)	³ He/ ⁴ He (Rc/Ra ^b)	He/ Ne
K-19	08/29/ 2023	4.2	2671	997,000	2100	349	0.68	30.8	0.82	396	0.0158	0.039	-12.0	-90.6	-3.8	-39.2	-5.69	294.0	9.05	9.16	23.38
K-20	08/31/ 2023	4.5	2636	994,000	5040	581	0.79	36.2	2.89	481	0.0766	0.0763	-12.0	-89.8	-4.1	-38.0	-4.87	297.3	9.39	9.43	64.40
K-21	08/30/ 2023	45.4	1113	1,000,000	116	19	0.24	10.9	1.93	1.2	0.0027	0.0027	-13.8	-97.2	-3.8	-41.1	-4.55	296.0	9.5	9.63	21.4
K-27	08/28/ 2023	37.8	1092	1,000,000	141	20	0.2	9.1	0.65	8	0.0045	0.0031	-11.8	-88.2	-3.5	-41.1	-3.62	297.2	n.a.	n.a.	n.a.
K-30	08/28/ 2023	14.3	2583	997,000	2100	588	0.57	26.7	0.52	412	0.0293	0.0269	-11.2	-89.1	-4.6	-39.1	-5.75	294.4	9.53	9.58	55.26
K-31	08/25/ 2023	0.6	2781	997,000	2160	505	0.83	40.4	0.69	501	0.194	0.0647	-12.4	-93.6	-3.6	-37.7	-6.04	292.8	8.73	8.96	10.8
K-32	08/29/ 2023	48.0	1095	1,000,000	130	47	0.18	8.5	0.35	8.9	0.0041	0.0045	-11.6	-88.5	-4.2	-41.3	-4.73	294.8	9.39	9.49	28.57
K-34	08/30/ 2023	14.9	2236	998,000	1440	589	0.5	22.7	0.52	262	0.0423	0.0178	-10.3	-87.2	-4.5	-39.8	-4.19	298.6	n.a.	n.a.	n.a.
K-36	08/28/ 2023	10.2	2607	996,000	2650	891	0.52	23.7	0.74	381	0.0243	0.0576	-10.6	-90.5	-4.9	-35.6	-3.93	296.1	10.05	10.14	30.36
K-38	08/28/ 2023	8.9	2035	997,000	1890	467	0.57	25.5	1.22	175	0.0221	0.0444	-11.7	-89.7	-4.4	-33.9	-2.78	297.4	10.34	10.4	52.96
K-40	08/24/ 2023	18.6	2762	994,000	5540	555	1.03	49.1	1.75	187	0.0513	0.0637	-11.7	-89.8	-4.4	-34.8	-4.09	296.6	n.a.	n.a.	n.a.
K-41	08/24/ 2023	6.3	2729	994,000	4970	511	0.64	30.8	1.65	389	0.1	0.0536	-11.9	-88.9	-4.7	-35.8	-4.48	298.9	9.3	9.44	19.15

^a R/Ra is the measured ³He/⁴He ratio divided by the ³He/⁴He ratio in air. ^b Rc/Ra is the air-corrected ³He/⁴He ratio divided by the ³He/⁴He ratio in air, calculated as (R/Ra – r)/(1 – r), where $r = (^4\text{He}/^{20}\text{Ne})_{\text{air}}/(^4\text{He}/^{20}\text{Ne})_{\text{meas}}$.

Chemical	Chemical (µmol mol ⁻¹) and isotopic composition of Krafla fumarole vapors.) and isoto	pic compos	sition of	Krafla	fumarol	e vapors	s. Isotop	es of C,	O and H,	, and Nar	e in ‰ vs.	V-PDB, V.	SMOW, ar	ıd atmospi	here, res	pectively. Th	e error for ⁴⁰ Ar/	Isotopes of C, O and H, and N are in ‰ vs. V-PDB, V-SMOW, and atmosphere, respectively. The error for "Ax/^o Ar ratios is ± 0.3.	~.
Sample Date	Date	()°()	T(°C) H ₂ O CO ₂ H ₂ S Ar N ₂	CO ₂	H_2S	Ar	N_2	CH4	H_2	Не	00	$\delta^{18} O_{\rm H2O}$	8D _{H2O}	$\delta^{13}C_{CO2}$	δ ¹³ C _{CH4}	$\delta^{15}N$	$^{40}\mathrm{Ar}/^{36}\mathrm{Ar}$	³ He/ ⁴ He (R/ Ra ^a)	$ {\rm CH_4} {\rm H_2} {\rm He} \qquad {\rm CO} \qquad \delta^{18} {\rm O}_{\rm H2O} \delta^{13} {\rm C}_{\rm CO2} \delta^{13} {\rm C}_{\rm CH4} \delta^{15} {\rm N} ^{40} {\rm Ar}/^{36} {\rm Ar} ^{34} {\rm E}/^4 {\rm He} \left({\rm R}/ ^{3} {\rm He}/^4 {\rm He} \left({\rm R}/ ^{3} {\rm He}/ \right) \right) \right) \right) $	He/ Ne
LKJ1	08/25/	97.2	97.2 998,000 1480 157 0.50 20	1480	157	0.50	20	10.1	62.8	0.0238	0.0324	10.1 62.8 0.0238 0.0324 -15.8 -107.1 -4.6 -43.9 0.86 304.6	-107.1	-4.6	-43.9	0.86		9.53	9.6	41.44
SUD1	08/27/ 2023	97.9	994,000 5390 679 0.23 10.4	5390	629	0.23	10.4	6.51	66.3	0.0417	0.0769	6.51 66.3 0.0417 0.0769 -16.5 -115.4 -4.3	-115.4	-4.3	-37.5 0.46 308.9	0.46	308.9	9.36	9.42	47.54
SUD2	08/30/ 2023	95.1	000,066	9260	9260 662 0.29	0.29	13	8.87 165	165	0.0695	0.150	-17.1	-112.5 -4.1	-4.1	-38.6 1.05		312.9	n.a.	n.a.	n.a.

Rc/Ra is the air-corrected 3 He/ 4 He ratio divided by the 3 He/ 4 He ratio in air, calculated as (R/Ra – r)/(1 – r), where $r = (^4$ He/ 2 0Ne) $_{air}$ /(4 He/ 2 0Ne) $_{meas}$. R/Ra is the measured ${}^{3}\text{He}/{}^{4}\text{He}$ ratio divided by the ${}^{3}\text{He}/{}^{4}\text{He}$ ratio in air.

for gas equilibrium in a single vapor phase, and

$$log\left(\frac{X_{CO,d}}{X_{H_2,d}}\right) = logK_{RWG,l} + logP_{CO_2} - log\left(\frac{B_{CO}}{B_{H_2}}\right) + log\left(\frac{D_{CO}^{\pm 1}}{D_{H_2}^{\pm 1}}\right)$$
(24)

for a two-phase fluid consisting of vapor and liquid coexisting at equilibrium. The logarithm of $K_{RWG,l}$ has been computed through SUPCRT92 (Johnson et al., 1992) using the thermodynamic database of Chase (1998) and its dependence on temperature has been fitted using a polynomial curve (Table S1).

To solve Eq. (24), we need to find an appropriate P_{CO2}-t dependence describing Krafla fluids. To this end, we used WATCH (Bjarnason, 2010) to reconstruct the P_{CO2} and temperature in the reservoir using the composition of geothermal well fluids from Gudmundsson and Arnórsson (2002) and Stefánsson (2014). This program solves mass and enthalpy conservation equations to calculate the concentration of reservoir fluids, starting from the liquid and vapor compositions separated at known pressure, temperature (e.g., using a mini Webre separator) and assuming a suitable reservoir temperature, which is the quartz temperature in our case (Arnorsson et al., 2007; Bjarnason, 2010). We considered two physical conditions of the aquifer as is often done in the literature (e.g., Stefánsson and Arnórsson, 2002; Stefánsson 2014, 2017). Condition 1 assumes only a liquid phase in the reservoir, whereas condition 2 assumes vapor and liquid coexisting at equilibrium in the reservoir. The presence of a vapor phase in the reservoir, either naturally occurring or formed through depressurization boiling of producing aquifers (Arnórsson et al., 1990, 2007), can better explain the excess-enthalpy measured in almost all the geothermal well fluid discharges of Krafla. Hence, we fitted the P_{CO2}-t (t in °C) data returned from WATCH using the two-phase (liquid and vapor) condition in the reservoir, according to

$$logP_{CO_2} = -12.851076 + 5.029718 \times logt$$
 (25)

For comparison, we also considered the P_{CO2} -t dependence (from Stefánsson and Arnórsson, 2002) described by the reaction 2 clinozoisite + 2 calcite + 3 quartz + 2 $H_2O = 3$ prehnite + 2 CO_2 (g) for activity of clinozoisite equal to 1 (pure endmember) and 0.3 (the average of clinozoisite in Icelandic geothermal systems; Sveinbjörnsdóttir, 1992; Table S2). In addition, we also used the equation of Chiodini and Cioni (1989) to calculate the P_{CO2} -T (T in K) relationship based on the RWG,1 reaction (Eq. 20; Table S2).

4. Results

4.1. Fluid compositions

Both fumarole and geothermal well fluids are dominated by H₂O, followed by CO2, H2S, and H2, whereas N2, CH4, Ar, He, and CO are less abundant (Table 1). Geothermal well fluids collected from the mini Webre separator are made up of coexisting vapor and liquid phases. The typical efficiency of Webre separators is 99.97 % or <0.03 % of brine carry over (Foong, 2005). We checked the efficiency of the vapor-liquid separation by analyzing the Na concentration in the steam condensate, whose high value would reflect mixing with the liquid phase, which has Na concentrations in the range 67.1–252 mg kg⁻¹ (Table S3). All samples show a negligible Na concentration (0.3–0.8 mg kg⁻¹; except K-27, with $Na = 5.3 \text{ mg kg}^{-1}$, and K-40 with $Na = 1.0 \text{ mg kg}^{-1}$; Table S3) and hence a fraction of liquid phase lower than 0.0049 (excluding K-40 and K-27, whose values are 0.015 and 0.022), that is, an efficient separation of the vapor and liquid phase. Almost all the samples (K-19, K-20, K-30, K-34, K-36, K-38, K-40, and K-41) are dominated by the vapor phase (steam fraction at the separator y in the range 0.64-0.99; Table S3) and show excess-enthalpy (2035–2781 kJ kg⁻¹ at 8.0–11.0 barg) up to K-31, which discharges a dry steam, whereas three samples (K-21, K-27, and K-32) display liquid-like enthalpy (1092-1113 kJ kg⁻¹ at 7.8-10.8 barg) and

Table 3

Temperatures of the largest feed zones of Krafla (T_{meas}) and temperatures estimated through solute and gas geothermometers. The equilibrium vapor fraction (y_e) and the total discharge enthalpy ($h_{d,c}$) calculated through an enthalpy balance using y_e and the vapor and liquid enthalpy at the temperature estimated through the $H_2O-H_2-CO_2-CO-CH_4$ gas system for wet-steam wells are also reported. The measured total discharge enthalpy (h_d) is also reported for comparison. T_{qtz} is estimated through WATCH (Bjarnason, 2010) using the relationship of Fournier and Potter (1982b), $T_{qtz/cha}$ using that of Cioni and Marini (2020), and $T_{Na/K}$ using that of Árnorsson et al. (1983). P_{CO2} is estimated through Chiodini and Cioni (1989) (Table S2).

Sample	T_{meas} [$^{\circ}$ C]	T H2O-H2-CO2-CO-CH4 [°C]	y_e	$h_{d,c}$ [kJ kg $^{-1}$]	h_d [kJ kg $^{-1}$]	P _{CO2} [bar]	$T_{\delta 13\mathrm{C}_{\mathrm{CO2}^{\circ}\mathrm{CH4}}}$ [°C]	T_{qtz} [$^{\circ}$ C]	$T_{qtz/cha}$ [$^{\circ}$ C]	$T_{Na/K}$ [$^{\circ}$ C]
K-19		297	0.73	2367	2671	0.31	185	261	264	270
K-20	306	284	0.90	2617	2636	0.49	204	272	275	249
K-21	269	272 ± 5	-	-	1113	6.93	170	254	263	244
K-27	296	288 ± 7	_	_	1092	1.20	168	240	248	214
K-30	308	285	0.93	2673	2583	0.20	199	248	274	270
K-31	282	320	0.81	2470	2781	0.40	197	_	_	_
K-32	314	315 ± 12	_	_	1095	1.58	171	253	257	238
K-34	322	281	0.56	2097	2236	0.21	192	257	264	250
K-36	317	307	0.70	2327	2607	0.47	236	264	268	268
K-38	313	303	0.26	1718	2035	0.79	249	239	248	214
K-40	286	280	0.42	1885	2762	1.05	238	198	200	276
K-41	277	276	0.90	2623	2729	0.42	225	-	262	245

low fractions of steam at collection (y = 0.17-0.19). The total discharge from these latter three wells is characterized by a higher proportion of water vapor (1000,000 μmol mol⁻¹; Table 1) and lower concentrations of CO₂ (116–141 μmol mol⁻¹), H₂S (19–47 μmol mol⁻¹), and H₂ (1.2–8.9 μ mol mol⁻¹) with respect to those of the excess-enthalpy fluids (H₂O = 994,000–998,000 μ mol mol⁻¹; CO₂ = 1440–5540 μ mol mol⁻¹; H₂S = 349-891 μ mol mol⁻¹; H₂ = 175-501 μ mol mol⁻¹). The chemical composition of fumarole gases (Table 1) span ranges similar to those of the excess-enthalpy geothermal fluids (Table 2). Their temperatures (95.1–97.9 $^{\circ}$ C; Table 2) are close to the local water boiling temperature, which is 98.2 °C at 550 m above sea level. The high concentration of water vapor, the relatively low concentration of CO₂ and H₂S, and the absence of acidic gas species typical of magmatic degassing (HCl, HF, and SO₂) fingerprints the hydrothermal origin of these fluids, which is also supported by the low concentration of Cl in the liquid phases (0.3–212 mg kg⁻¹; Table S3) collected at the separator for the wet-steam well fluids. As these fluids show relatively low gas concentrations and salinity, we can consider the thermodynamic properties of pure water without expecting significant deviations.

4.2. Hydrothermal temperature and P_{CO2} estimated through the $H_2O\text{-}H_2\text{-}CO_2\text{-}CO\text{-}CH_4$ system

The concentration of H2O, H2, CO2, CO, and CH4 in the total well discharge and fumarole vapors is sensitive to the thermodynamic conditions of the geothermal system (T, P, and redox), and hence it can be used to gain insights on such properties. To this end, we compared the concentrations of these gas species with theoretical grids of vapor/liquid equilibrium, or the coexistence of both phases (Section 3.4; Figs. 3, 4b,c). These theoretical grids describe gas equilibrium in a single vapor and liquid phase (Figs. 3, 4b,c). In the region between these curves, we model either adiabatic boiling and single-step separation of vapor (model 1 in Section 3.4; Fig. 3a, c, e; Eq. (8)-(12)) or coexistence of equilibrium vapor and liquid in the geothermal reservoir (model 2 in Section 3.4; Fig. 3b, d, f; Eqs. (14)-(18)). Both models show that excess enthalpy fluids cluster close to the equilibrium vapor line (Fig. 3). The liquid-like enthalpy fluids (K-21, K-27, and K-32) plot instead close to the equilibrium liquid line in model 1 (Fig. 3a, c, e), which reports the vapor composition of the well fluids (in µmol mol⁻¹, Table S3), whereas they are shifted beyond the liquid line in model 2 (Fig. 3b, d, f), which considers the total well discharges (Table 1). In both models, the excessenthalpy fluids cluster in a narrow region of temperatures, which span the 300–350 $^{\circ}\text{C}$ range in model 1 (Fig. 3c, e) and 272–320 $^{\circ}\text{C}$ in model 2 (Fig. 3d, f, 5a; Table 3).

The $P_{\rm CO2}$ estimated with the equation of Chiodini and Cioni (1989) (Table 3) and the temperature returned from the $H_2\text{O-}H_2\text{-CO}_2\text{-CO-}\text{CH}_4$ gas system (model 2) for excess-enthalpy fluids (all except K-21, K-27,

and K-32; Table 3) overlap the P_{CO2} -temperature dependence calculated through linear regression of WATCH outputs of the literature data (Gudmundsson and Arnórsson, 2002; Stefánsson, 2014) for two-phase aquifer fluids (Fig. 4a; Eq. 25; Section 3.4.1). Such values are instead lower than those returned by modeling with WATCH a single-phase, liquid aquifer, which appear to be explained by the clinozoisite-calcite-quartz-phrenite mineral buffer for $a_{Czo} = 1$ and $a_{Czo} = 0.3$ (Fig. 4a; Stefansson and Arnorsson, 2002).

4.3. Origin of the fluids

4.3.1. Water isotopes

Oxygen and hydrogen isotopes of both liquid and vapor (steam condensate) of the wet-steam well fluids, reported in delta notation versus V-SMOW, show compositions bracketed between the local meteoric water and a component with more positive $\delta^{18}O_{\rm H2O}$ at nearly constant $\delta D_{\rm H2O}$ (Fig. 6a). The liquid phase collected at the mini Webre separator has heavier $\delta^{18}O_{\rm H2O}$ values compared to the vapor phase (Fig. 6a). The isotopic composition of water on a total discharge basis spans a range between the local meteoric water and the water reinjected into the geothermal system, except the K-21 fluid, which appears to reflect a meteoric water with lighter isotopes than the local rain water of Krafla (Fig. 6b). The steam condensates of the fumarolic vents show depleted isotopes with respect to the cluster of total discharge data, but also the K-21 fluid (Fig. 6b).

4.3.2. N2, He, Ar, CO2, and their isotopes

Nitrogen, helium, and argon composition of Krafla fluids show the concurrent contribution of He-poor air saturated water (ASW, or groundwater) and a He-rich magmatic component (Fig. 7). Air corrected (Rc) He isotope ratios ($^3\text{He/}^4\text{He}$) of both fumarole and geothermal well fluids span from 8.96 to 10.40 Ra (Table 1, 2), with average of 9.57 \pm 0.40 Ra, which is slightly higher than that of the upper mantle (8 \pm 1 Ra; Farley and Neroda, 1998). At first glance, nitrogen isotopes of the geothermal well fluids (^{81}N from -2.78 to -6.04 %; Table 1) also appear to fingerprint the value of the upper mantle (-5 ± 2 %; Marty and Dauphas, 2003), whereas fumarole vapors show $\delta^{15}\text{N}$ (0.46–1.05 %; Table 2) slightly higher than the atmospheric values (0 %). The C isotope composition of CO₂ of fumarole and geothermal well fluids span the range between -4.9 and -3.5 %, with average (\pm 1 σ) of -4.2 ± 0.4 % (Tables 1, 2), approaching the value of the upper mantle (-5 ± 1 %; Marty and Zimmermann, 1999).

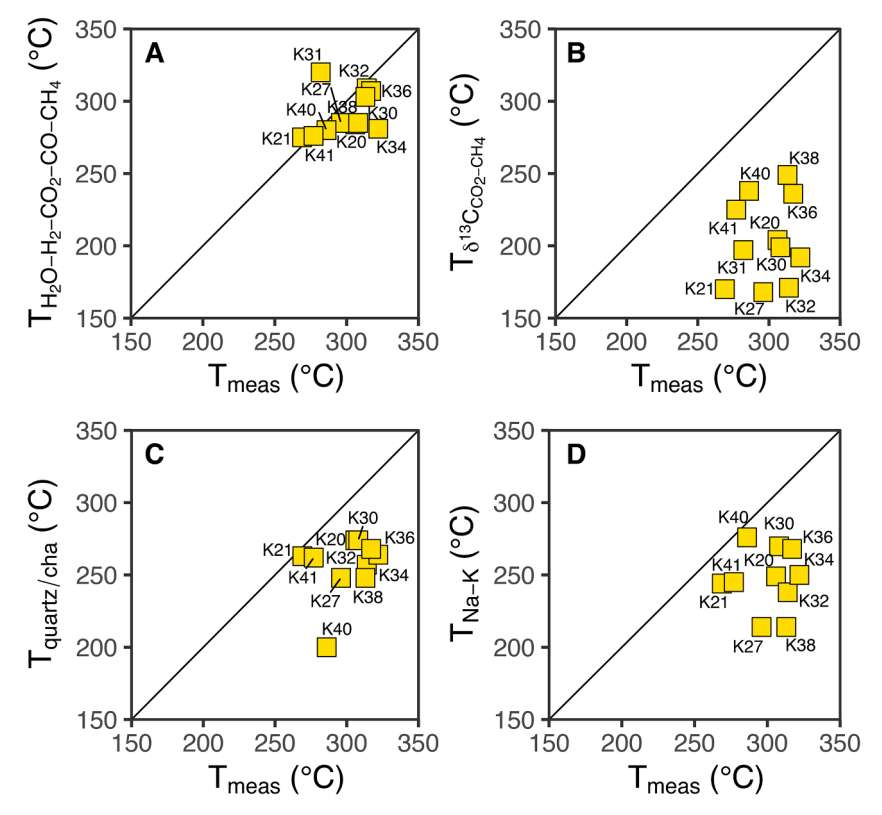


Fig. 5. Temperatures estimated through the (a) $H_2O-H_2-CO_2-CO-CH_4$ gas system for wet-steam wells (Section 3.4), (b) C isotope exchange between CO_2 and CH_4 , quartz/chalcedony (Cioni and Marini, 2020), and (d) Na-K (Arnórsson et al., 1983) plotted against the temperatures of the largest productive feed zones (black dashed line in Fig. 2).

5. Discussion

5.1. Gas equilibrium in the H₂O-H₂-CO₂-CO-CH₄ system reveals aquifer temperatures and secondary processes affecting fluid composition

Krafla wet-steam well fluids show in most cases an excess of enthalpy, which is ascribed either to the natural coexistence of vapor and liquid in the aquifer or to the development of steam zones due to depressurization and boiling of liquids during production. The presence of liquid and vapor phases in the reservoir prevented us from using model 1 in Section 3.4, which assumes the presence of a single liquid phase in the geothermal aquifer, adiabatic boiling of the liquid, and vapor separation in a single-step (Chiodini and Marini, 1998). In contrast, model 1 can adequately explain fumarole gases. Indeed, fumarolic vents naturally emit steam at ~100 °C and atmospheric pressure, consistent with boiling process of a single liquid phase at depth. Suðurhlíðar (SUD1, SUD2) and Leirhnjúkur (LKJ1) fumarole vapors appear to be generated from a common original liquid at 322 °C, which cooled down and boiled at temperatures between 100 and 300 °C (Fig. 3a, c, e). Alternatively, Suðurhlíðar fumarole vapors (SUD1, SUD2) might derive from a two-phase aquifer with temperatures around 282 °C (model 2 in Section 3.4; Fig. 3b, d, f), which approach those estimated for the same geothermal subfield using well fluids (Fig. 2; see below). The high enthalpy of geothermal well fluids is instead better explained by equilibrium coexistence of a vapor and liquid phase in the reservoir (model 2 in Section 3.4; Fig. 3b, d, f), despite other contributing processes, such as liquid phase segregation, cannot be excluded (see Section 3.4). Notably, the productive aquifers feeding the excess-enthalpy fluids may have very high fractions of equilibrium vapor (y_e up to 0.93; Table 3) coexisting with the liquid phase (Fig. 3d, f), justifying the presence of almost dry steam at sampling condition. The equilibrium temperatures of these excess-enthalpy fluids estimated through the redox-independent grid (Fig. 3d, f) varies from 272 °C to 320 °C (Table 3), whereas those estimated through the redox-dependent grid (Fig. 3b) are slightly lower. As the grid geometry of Fig. 3b critically depends on the redox buffer employed, the redox-independent grids (Fig. 3d, f) return reservoir temperature estimates affected by less uncertainty. Moreover, it is unlikely that a unique redox buffer controls the whole set of samples. The total enthalpy of these fluids in the reservoir $(h_{d,c} \text{ in Table 3})$ – calculated through an enthalpy balance based on y_e and the vapor and liquid enthalpy at the estimated reservoir temperature – is moderately lower than the measured total discharge enthalpy, h_d (Table 1; Fig. S1), for most excess-enthalpy wells with differences, Δh $= h_d - h_{d,c}$, ranging from 18.5 to 316 kJ kg⁻¹ around an average value (\pm 1σ) of 210 \pm 112 kJ kg⁻¹. The only exceptions are wells K-30 and K-40, with Δh of -90 and 877 kJ kg⁻¹. In spite of possible uncertainties both in the measurement of h_d and in the calculation of $h_{d,c}$, the prevailingly positive values of Δh might be due to liquid phase segregation, that is, partial retention of liquid water in the aquifer, because of its adhesion onto the surfaces of mineral grains by capillary forces, whereas the vapor phase is totally transferred from the aquifer to the well (Arnórsson and Stefánsson 2005; Arnórsson et al. 2007, 2010).

The shift of the liquid-like enthalpy well fluids (K-21, K-27, and K-32) is less straightforward to understand, as these samples plot beyond not only the equilibrium liquid line, but also the grid of residual liquids that have lost vapor through boiling (blue grid in Fig. 3b, d, f). As water is the dominant component of the fluids, steam condensation or steam/liquid water addition can significantly affect gas ratios involving $\rm H_2O$. The low $\rm H_2/H_2O$ ratio in Fig. 3b suggests addition of water to the K-21, K-27, and K-32 discharges. However, inspection of Fig. 3d, f shows that as an alternative to $\rm H_2O$ addition, a variation in the $\rm CO/H_2$ ratio, which is a $\rm P_{\rm CO2}$ indicator (Chiodini and Cioni, 1989), may contribute to the shift of the liquid-like enthalpy samples. To separately consider how much the $\rm P_{\rm CO2}$ variation and $\rm H_2O$ addition/condensation affect the compositional shift of these samples, we computed the equilibrium composition fixed by the RWG reaction for liquid water (see Section

3.4.1 for further details) and we reported the theoretical vapor-liquid grids in Fig. 4b. In addition to temperature, this grid also depends on the P_{CO2} . The P_{CO2} -temperature dependence used in this grid has been calculated through linear regression of WATCH (Bjarnason, 2010) outputs of the literature data (Gudmundsson and Arnórsson, 2002; Stefánsson, 2014) for two-phase aquifer fluids (Fig. 4a; Eq. 25; Section 3.4.1). Fig. 4b shows that the equilibrium temperatures are still bracketed in a narrow range as in Figs. 3d, f, suggesting the horizontal scatter of sample points is controlled by variation in the P_{CO2} . By including the error of the P_{CO2} -t fit (the 68.3 % prediction band, that is, one standard deviation for a Gaussian distribution; red curves in Fig. 4a), all the samples can be explained by the theoretical grids, except K-21 (Fig. 4c). Notably, the shift of samples K-27 and K-32 observed in Fig. 3d, f has significantly decreased in Fig. 4b, approaching the K-40 and K-38 samples, whereas K-21 has maintained a larger variation. Therefore, the water addition appears to significantly affect the composition of both K-27 and K-32 samples, whereas the K-21 fluid appears to be also controlled by a higher P_{CO2}. Such a P_{CO2} seems consistent with that fixed by the mineral buffer clinozoisite-calcite-quartz-phrenite for clinozoisite activity between 0.3 and 1 (Fig. 4a, S2), which, according to Stefánsson and Arnórsson (2002), controls the P_{CO2} in the geothermal waters of Iceland. A comprehensive study of different vapor-liquid grids is needed to discern the processes affecting geothermal well discharges, as the solely inspection of the grid of Fig. 3b would only point out steam addition, without underscoring the P_{CO2} effect (Fig. 3d, f, 4b,c).

Water addition to K-27 and K-32 fluids involves liquids with a lowgas concentration (Fig. 3d, f), consistent with both reinjection fluid and liquids located at shallower depths with respect to the main productive aquifer. For example, the composition of the K-32 fluid might be explained by the addition of a 0.97 fraction from nearly pure water with minimal gas content to a K-38-like fluid (red-pink arrow in Figs. 3d, f). Although this process provokes a large variation in the H₂O/CO₂ ratio, the temperature estimates are nearly unaffected (Fig. 3d, f). By horizontally shifting the K-21, K-27, and K-32 samples within the grid of vapor/liquid coexistence in Fig. 3d, or by applying a diagonal shift with a slope of -4 in Fig. 3f, the temperatures and the associated errors considering the range of y_e spanning from 0.03 to 1 are 272 \pm 5 $^{\circ}$ C for K-21, 288 \pm 7 °C for K-27, and 315 \pm 12 °C for K-32. Fractions of equilibrium vapor lower than 0.03 would increase the error associated with these temperature estimates. However, these very low fractions are unlikely for these samples showing a liquid-like enthalpy, as they would reflect a complete vaporization of the liquid phase and hence a very energetic process, such as a steam-driven eruption.

5.2. CO-based temperatures closely match the temperature of the main geothermal aquifer of Krafla and its evolution over time

The temperatures estimated through the H₂O-H₂-CO₂-CO-CH₄ gas system for wet-steam well discharges are compared with the outcomes of other geothermometers commonly employed for geothermal energy exploration, together with the natural state temperature-depth profiles (solid black line) and the temperatures of the main feed zones (dashed lines; Fig. 2; see Section 2 for details on the natural state temperaturedepth profiles). These production zones are the largest encountered downhole but a few more feed zones of less importance and extent were also encountered during drilling operations. The grey area in Fig. 2 indicates the section of the well below the casing, which is completed with the liner and hence is the area from which fluids potentially enter the borehole, unless the casing is affected by cracking or corrosion. It is important to point out that both the formation and feed zone temperatures (Fig. 2) were estimated based on data acquired at well completion, that is, between 1982 (K-19, K-20, and K-21) and 2016 (K-41). Hence, they do not account for temporal variations due to fluid exploitation.

The temperatures based on the $H_2O-H_2-CO_2-CO-CH_4$ gas system better approach the temperatures of the main feed zones with respect to the other geothermometers (Fig. 2, 5), and in a few cases they are almost

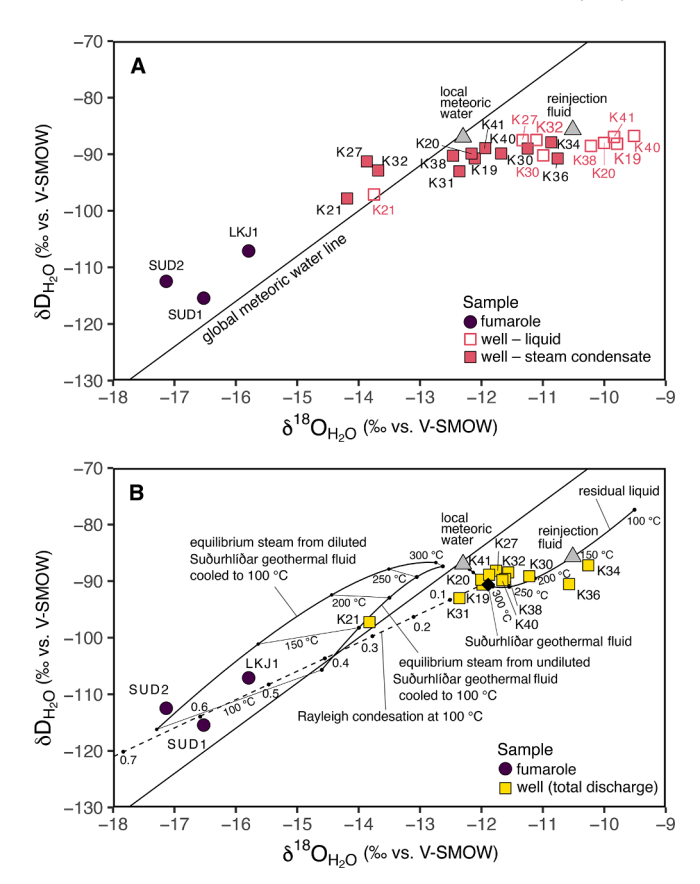


Fig. 6. Hydrogen isotopes plotted against oxygen isotopes of water of fumarole and wet-steam well fluids, including both (a) liquid and vapor phases collected at the mini Webre separator and (b) total discharges. (b) Curves of steam separation at $100-300\,^{\circ}\text{C}$ from the boiling of an original fluid (black diamond) at $322\,^{\circ}\text{C}$, cooled down by the interaction with meteoric water are reported (black solid). Rayleigh condensation at $100\,^{\circ}\text{C}$ of the original fluid (black diamond) is also reported (dashed line).

identical, such as for K-36, K-38, K-40, and K-41. The geothermometer based on the C isotope exchange between CO₂ and CH₄ returned in most cases temperatures far lower than those of the largest feed zones (red line; Fig. 2, 5b), showing a clear disequilibrium, as also pointed out by other authors (e.g., Beaudry et al., 2021; Stefánsson et al., 2024). Temperatures estimated by WATCH (Bjarnason, 2010) with the silica geothermometer (Fournier and Potter, 1982b) for two-phase well fluids are lower than both those estimated with the H₂O-H₂-CO₂-CO-CH₄ gas system and those measured in the largest feed zones (Table 3). By using the quartz/chalcedony equation calibrated by Cioni and Marini (2020), which describes the solubility of quartz crystals of average grain size and corresponds to the central tendency of SiO2-based geothermometers proposed by different authors, the equilibrium temperatures are slightly higher but still lower than those of the primary aquifers (blue line; Figs. 2, 5c). Similar to quartz, the Na-K concentration in the liquid of wet-steam well fluids (Table S3) records lower aguifer temperatures (green line; Fig. 2, 5d; estimated through the equation of Arnórsson et al., 1983, which was calibrated with Icelandic fluids). The lower temperatures recorded by liquid phases suggest mixing of fluids originating from different production zones. While the vapor phase appears to be primarily sourced by the largest feed zones, reflecting the main high-temperature, two-phase aquifer of Krafla, the liquid phase may derive from minor, cooler aquifers located at shallower depths.

The close match between the temperatures estimated in this work and those of the largest feed zones suggests gas equilibrium in the $H_2O-H_2-CO_2-CO-CH_4$ system and coexistence of vapor and liquid in the main, deeper productive aquifer. Previous works on Icelandic fluids did not

exclude local equilibrium between some of these gases, but they did not support the overall equilibrium between H2O, H2, CO2, and CH4 (e.g., Stefánsson and Arnórsson, 2002). Our findings mainly stem from the introduction of carbon monoxide (CO) analysis, which has been only recently reported for the Icelandic fluids by Stefánsson et al. (2024), supporting an overall disequilibrium between H2O, H2, CO2, CO, and CH₄. However, these authors only considered aqueous CO equilibrium in a single liquid phase according to the RWG reaction (Eq. (5)) and the Sabatier-Senderens reductions $(CO+3H_2=CH_4+H_2O$ CO₂+4H₂=CH₄+2H₂O, which are the SS3 and SS4 of Marini et al., 2022; SS4 is Eq. (7) in this work), without exploring gas equilibration in a vapor phase or in a vapor plus liquid, two-phase system. This assumption of gas equilibration in a single liquid phase is at variance with the excess enthalpy of the Krafla well discharges (Arnorsson et al., 2007). In this study, we presented the RWG and SS4 reactions (Fig. 3e, f), besides the RWG and CCC pair (Fig. 3c, d), to independently assess the impact of CO and CH₄ on temperature and vapor fraction estimates, as CO participates in both RWG and CCC reactions. Both applications (Fig. 3c, d, e, f) suggest attainment of gas equilibrium in the vapor-liquid coexistence field for Krafla samples.

The increase in flow and decrease in enthalpy of well discharges at Leirbotnar (K-27 and K-32) over time appears to result from the inflow or mixing of colder fluid with that of the main (deeper) aquifer (Mortensen et al., 2015). For example, the total discharge enthalpy of K-32 has experienced a notable decline of 1000 kJ kg⁻¹ from 2002 to the present (Weisenberger et al., 2015). Notably, this hypothesis is supported by the addition of water suggested for the same samples by the H₂O-H₂-CO₂-CO-CH₄ gas system (Fig. 3d, f). It is noteworthy that K-27 and K-32 wells are the closest to the reinjection well K-26 (Fig. 1b), suggesting that the reinjected water could be a potential source of this gas-poor liquid added to the deeper fluid. Alternatively, the downflow of water from shallower, colder aquifers may also account for this addition (Fig. 3d, f). In this regard, Na-K and quartz/chalcedony concentration of K-27 and K-32 indicates temperatures comparable to those of the shallow liquid aquifer in the isothermal zone (Fig. 2), suggesting downflowing from this part of the system. Addition of a gas-poor liquid is further corroborated by the temporal decrease in the enthalpy of K-21 (Fig. 3d, f), whereas the enthalpy of the remaining well discharges has remained relatively stable over time (e.g., K-20, K-30, K-31, K-36, K-40, and K-41; Mortensen et al., 2015; Weisenberger et al., 2015).

5.3. The meteoric recharge and the reinjection fluid dominate the composition of the geothermal fluid with a minor contribution from magmatic outgassing

5.3.1. Water isotopes

The water isotopes of the total geothermal well discharges ($\delta^{18}O_{H2O}$ $=-11.7\pm0.9$ % on average \pm 1 σ) are dominated by meteoric water $(\delta^{18}O_{H2O} = -12.3 \text{ %; Sveinbjörnsdóttir et al., 1986; Darling and}$ Ármannsson, 1989), whereas the H₂O contribution from magmatic outgassing appear negligible, not only for $\delta^{18}O_{H2O} = 5-10$ % (Giggenbach, 1992), but also for the low δ^{18} O values of Krafla lavas (1.0-4.5 % for both unaltered rhyolites and basalts; Nicholson et al., 1991; Pope et al., 2013; Troch et al., 2020) and the rhyolite tapped during the drilling of the IDDP-1 well (+3.2 \pm 0.2 %; Elders et al., 2011) (Fig. 6). The horizontal shift towards positive $\delta^{18}O_{H2O}$ at nearly constant δD_{H2O} (Fig. 6b) is consistent with both O-isotopes exchange between the geothermal fluid and the host rock (e.g., Stefánsson et al., 2017) and mixing of the local meteoric water recharge with the fluid reinjected into the geothermal system. All the fluids belonging to the main production area of Krafla are bracketed in this meteoric-reinjection fluid mixture, whereas the only sample collected from the peripheral part of the main upflow zone (K-21) has lighter isotopes akin to a different meteoric component. However, this variation can be partly affected by the presence of condensed steam into the separated liquid phase due to the high pressure at which K-21 was sampled, as indicated by the similar isotopic

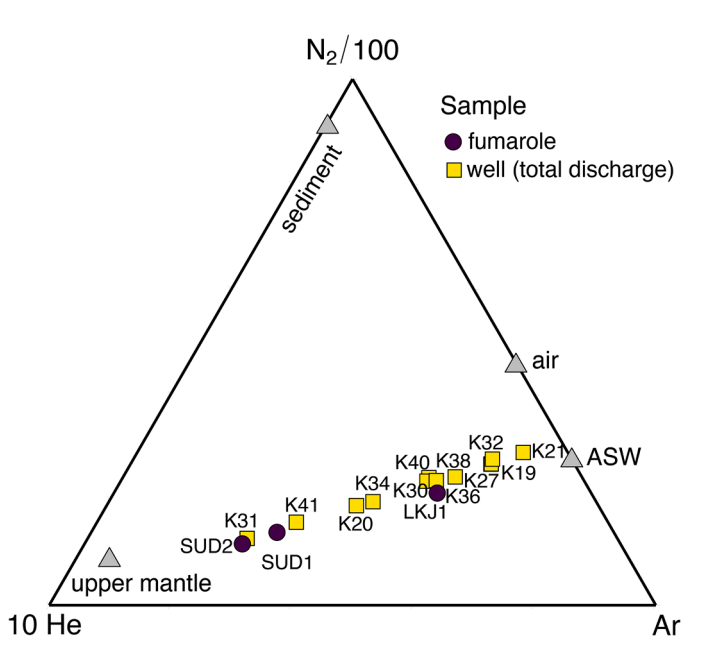
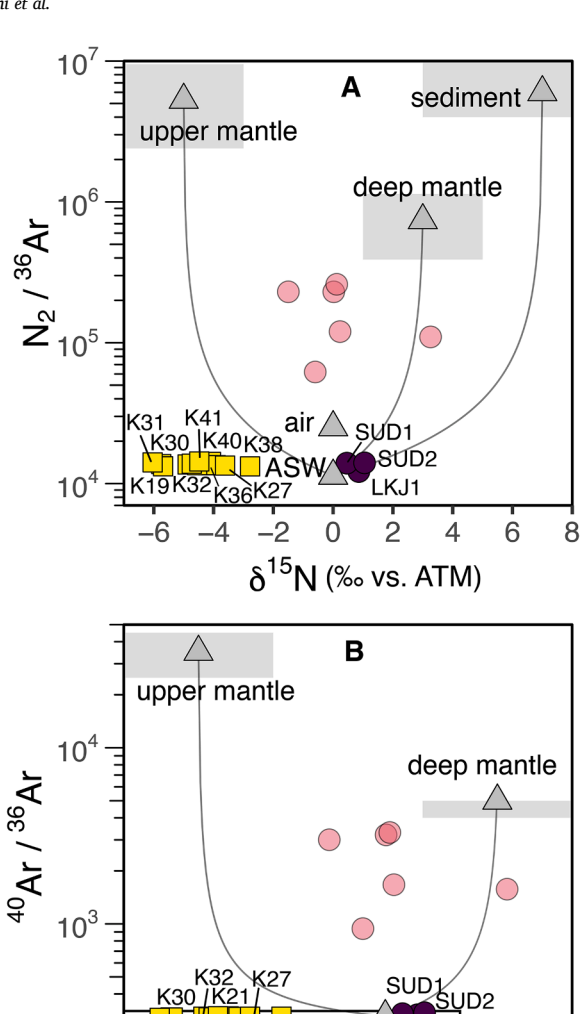


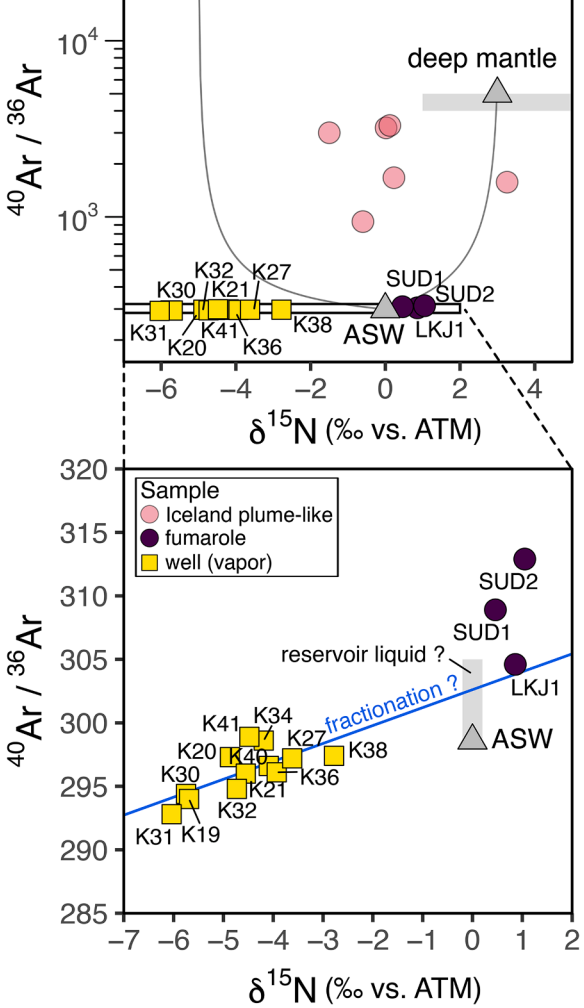
Fig. 7. N₂-He-Ar ternary diagram showing that both fumarole and wet-steam fluids are mixtures of air saturated water (ASW) and magmatic fluids.

values of the respective liquid and vapor phase (Fig. 6a). The lighter values of fumarole vapors (Fig. 6) might be consistent with steam separation through boiling of geothermal liquids. To model this process, we used the equations of Giggenbach and Stewart (1982). As most of the fumaroles are located in Suðurhlíðar, we used the average of the fluids sampled in this subfield (K-19, K-20, K-30, K-31) as the original fluid composition (black diamond in Fig. 6b). By assuming an equilibrium temperature of the original fluid of 322 °C, as inferred through the H₂O-H₂-CO₂-CO-CH₄ gas system for fumaroles (model 1 in Section 3.4; Fig. 3a, c, e), we modeled the composition of the equilibrium steam separated from this fluid at different separation temperatures (100-300 °C; Fig. 6b). As hydrothermal fluids may interact with colder groundwater during their upflow towards the surface, we also modeled steam separation from a mixture of the original geothermal fluid with the local meteoric water at 10 °C (Fig. 6b). Fumarole vapors are explained by steam separation at ~100-120 °C from an original geothermal fluid at 322 °C that mixes with the local meteoric water and cools down (Fig. 6b). Alternatively, assuming that fumarole vapors originate from a two-phase aquifer at around 282 °C (model 2 in Section 3.2; Fig. 3b, d, f; Section 5.1), Rayleigh condensation at 100 °C (dashed line in Fig. 6b; see Eq. (19)-(21) in Marini and Fiebig, 2005) of this original fluid (black diamond) also appears to fit the isotopic compositions of the fumarole vapors. Such a process can reasonably occur in the subsurface, and is supported by the low-flux of the fumarolic vents, which is akin to that of steaming grounds. Both processes can also explain the variation in water concentration within fumaroles, as indicated by the H2O-H2-CO2--CO-CH₄ gas system (Fig. 3a, c, e). While this variation may impact the separation temperature estimates (Fig. 3a, c, e) or the equilibrium vapor fractions (Fig. 3b, d, f), the equilibrium temperature of the aquifer remains relatively constant.

5.3.2. Nitrogen, argon, and their isotopes

The relative concentrations and the stable isotopes of nonreactive gas species can track the sources of the geothermal fluids (such as magmatic, atmospheric, or crustal), as these are characterized by distinct isotopic signatures. To our knowledge, few studies reported N isotopes of Icelandic fluids (Sano et al., 1985; Ármannsson et al., 1989; Marty et al., 1991; Óskarsson et al., 2015; Labidi et al., 2020) and only Sano et al. (1985) and Ármannsson et al. (1989) analyzed the δ^{15} N of four well discharges of Krafla (K-7, K-8, K-15, and K-22), reporting





(caption on next column)

Fig. 8. (a) $N_2/^{36} Ar$ and (b) $^{40} Ar/^{36} Ar$ ratios plotted against nitrogen isotopes of Krafla vapor phases. $\delta^{15} N$ shows similar values to that of the upper mantle but lower $N_2/^{36} Ar$ (a) and $^{40} Ar/^{36} Ar$ (b). The blue line in the enlargement of (b) is a simple linear regression through the well discharge data, which could reflect a mass dependent fractionation of a reservoir liquid with ASW-like composition. The canonical values of the upper mantle (Bini et al., 2022 and references therein), plume-type mantle (Marty and Dauphas, 2003), sediment (Sano et al., 2001), air, and air-saturated water (ASW), that is, groundwater, are reported for comparison. Subglacial glasses from Iceland (from a quarry in Dagmalafell, Midfell, 1 km east of Lake pingvallavatn) showing a plume-like mantle origin from Marty and Dauphas (2003) are also reported as pink circles.

positive values (from 0.2 to 4 % vs. atmosphere). The new isotope data provided in this study can thus help us to gain insights into the sources and processes influencing Krafla fluids.

Nitrogen isotopes of the well vapor phases show negative values $(\delta^{15}N \text{ from } -2.78 \text{ to } -6.04 \text{ }\%; \text{ Table } 1) \text{ different from those of Sano et al.}$ (1985) but similar to that of the upper mantle (-5 \pm 2; Marty and Dauphas, 2003), suggesting N₂ contribution from magmatic outgassing. However, both $N_2/^{36}$ Ar and 40 Ar/ 36 Ar ratios are far lower than those of the mantle (Fig. 8a, b). Notably, the 40 Ar/ 36 Ar ratio of well vapor phases linearly decreases with the δ^{15} N values (Fig. 8b), approaching values even lower than that of the air-saturated water (ASW, 298.6; Lee et al., 2006) and suggesting similar fractionation processes controlling both Ar and N isotopes. By analyzing the relationships between Ar and N isotopes in well vapors and their concentrations in the total discharges (Fig. 9), three distinct clusters of samples emerge in both diagrams. Fumarole data display δ^{15} N and N₂ concentrations (δ^{15} N = 0.46–1.05 % and $N_2 = 10.4-20 \,\mu\text{mol mol}^{-1}$), as well as $^{40}\text{Ar}/^{36}\text{Ar}$ and Ar concentrations $(^{40}\text{Ar}/^{36}\text{Ar} = 304.6 - 312.9 \text{ and Ar} = 0.23 - 50 \,\mu\text{mol mol}^{-1})$ that are comparable or slightly higher than those of the ASW ($\delta^{15}N=0$ ‰, $^{40}\text{Ar}/^{36}\text{Ar} = 298.6$, $N_2 = 11.9 \text{ }\mu\text{mol mol}^{-1}$, and $Ar = 0.28 \text{ }\mu\text{mol mol}^{-1}$; Fig. 9). This composition suggests contributions from shallow groundwater or geothermal fluids dominated by meteoric recharge, where ⁴⁰Ar is gained through the fractured hosting rock. The liquid-enthalpy well discharges (K-21, K-27, and K-32) are similar to, or appear to have undergone vapor loss relative to a liquid reservoir with an ASW-like composition. This trend could be consistent with the addition of a degassed liquid, such as the reinjected fluid (see also Section 5.2). On the contrary, the excess-enthalpy discharges suggest an addition of vapor that is rich in Ar and N₂ but depleted in 40 Ar/ 36 Ar and δ^{15} N relative to the reservoir liquid (Fig. 9). This vapor addition could also influence the LKJ1 fumarole (Fig. 9).

Enrichment of lighter isotopes of Ar, N, Ne, Kr, and Xe – leading to isotope ratios even lower than the ASW value – has been documented in geothermal fluids from various systems worldwide, including Iceland (Marty et al., 1991; Bekaert et al., 2023), Japan (Nagao et al., 1979, 1981), and the United States (Bekaert et al., 2023). This mass dependent fractionation can be explained by the mutual diffusion of trace gases in a major gas (Marty, 1984), recently termed diffusive transport fractionation (Bekaert et al., 2023). In this process, atmospheric inert gases trapped in rock pore spaces or degassed from groundwater are flushed by the geothermal fluid upflow (Marty, 1984). Due to the faster diffusion rate of lighter noble gases through the main gas phase of the geothermal upflow (e.g., H2O or CO2), the upflowing vapor becomes enriched in lighter isotopes (Marty, 1984; Bekaert et al., 2023). Marty et al. (1991) hypothesized this diffusion process to explain the negative range of $\delta^{15}N$ from -0.2 to -10.4 % of the geothermal fluid of the Hengill area, Iceland, as an alternative to mantle degassing. Another process that is thought to produce negative $\delta^{15}N$ in geothermal fluids is the repeated degassing of N₂ from geothermal water (Labidi et al., 2020). However, due to the small depletion in $\delta^{15}N$ of the N_2 dissolved in the liquid phase after degassing (-0.5 % at 60 °C; Lee et al. (2015)), this process would require approximately 99 % exsolution of N2 from ASW to account for an observed $\delta^{15}N$ of N_2 of -5 % (Labidi et al., 2020). Both these fractionation processes may be exacerbated in the case of the Krafla geothermal

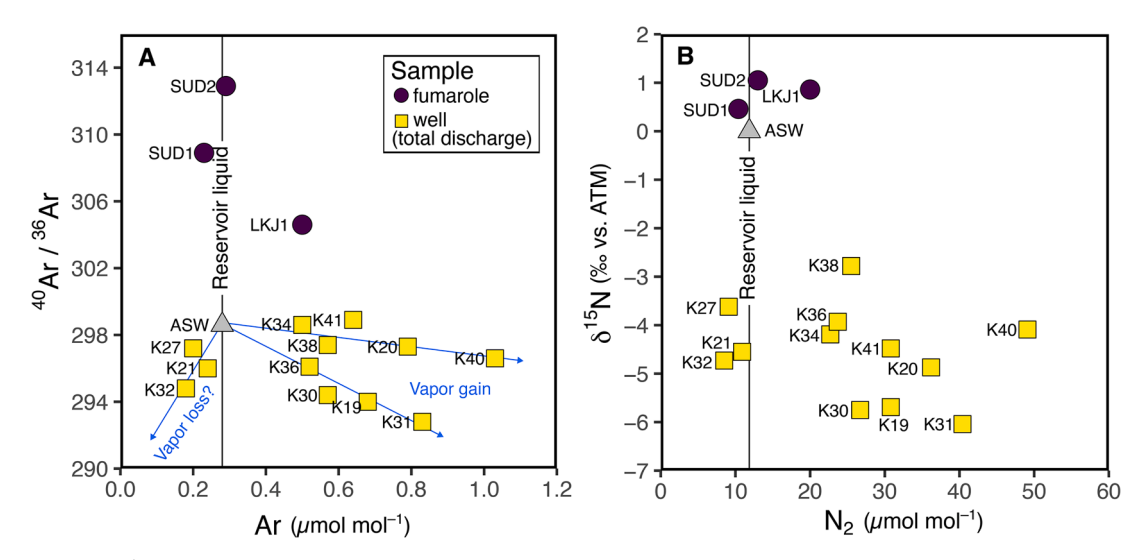


Fig. 9. Ar isotope ratio and $\delta^{15}N$ of Krafla vapor phases plotted against the Ar (a) and N_2 (b) concentrations in the total discharges, respectively. Hypothetical trends of vapor gain/loss with respect to an ASW-like reservoir liquid are depicted by blue arrows.

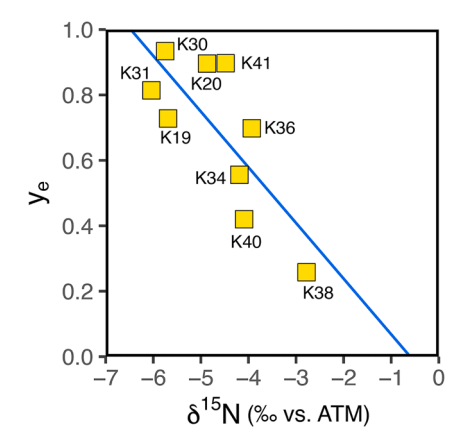


Fig. 10. Fraction of equilibrium vapor (y_e) estimated through the $\rm H_2O-H_2-CO_2-CO-CH_4$ gas system for wet-steam wells (Section 3.4) plotted against nitrogen isotopes of well fluids. The inverse correlation between y_e and $\delta^{15}N$ (blue regression line) suggest that the aquifers that have developed more extensive vapor zones are characterized by the strongest depletion in $\delta^{15}N$ possibly due to fractionation of an ASW-like reservoir fluid (0 ‰).

system, where nearly 50 years of exploitation have resulted in extensive depressurization boiling, large fluid upflow, and the formation of vapor zones within the reservoir. To this respect, it is interesting to note that the $\delta^{15}N$ value of excess-enthalpy well discharges decreases as the fraction of equilibrium vapor (ye) estimated with the H2O-H2-CO2--CO-CH₄ gas system increases (Fig. 10). Additionally, other significant fractionation processes during geothermal reinjection cannot be ruled out, as reinjection began at Krafla in 1999. Panichi (2004) documented notable changes in the N2, He, and Ar concentrations of the well discharges of Larderello (Fig. 7 in Panichi, 2004), Italy, following the onset of fluid reinjection in 1979. While these processes may each contribute to varying extents to the observed trends in 40 Ar/ 36 Ar and δ^{15} N isotopes at Krafla (Figs. 8b, 9), complicating their interpretation, these patterns are more likely indicative of the fractionation of an ASW-like reservoir rather than a simple mixing between different Earth's reservoirs, such as ASW and mantle.

5.3.3. Carbon dioxide, helium, and their isotopes

If on one hand H_2O , N_2 , and Ar isotopes reveal an atmospheric-like source consistent with the meteoric recharge and reinjection fluid (Figs. 6–9), on the other hand, CO_2 and He isotopes (–4.2 \pm 0.4 % and

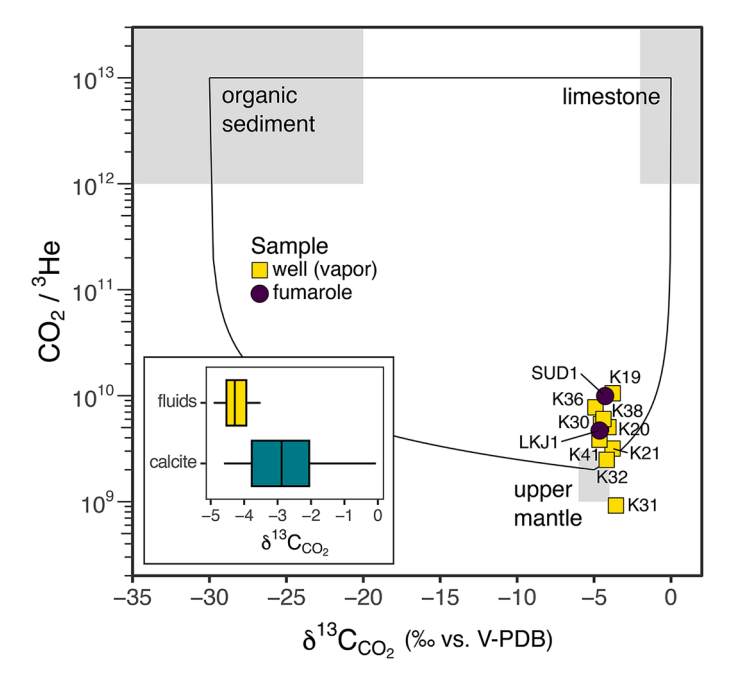


Fig. 11. ${\rm CO_2}{}'^3{\rm He}$ ratio plotted against carbon isotopes of ${\rm CO_2}$ of fumarole and geothermal well fluids. All the samples point out a magmatic origin. However, the $\delta^{13}{\rm C}$ of the ${\rm CO_2}$ in the current geothermal fluids is more negative than that of the Icelandic mantle signature (–2.5 \pm 1.1 ‰; Barry et al., 2014), which is instead preserved in calcite samples recovered from drill cuttings (box plots in the inset; Bini et al., 2024). As magmatic outgassing progressively fractionates $\delta^{13}{\rm C}_{{\rm CO2}}$ towards negative values, the current degassing can be sustained by a degassed magma, whose low $P_{{\rm CO2}}$ prevents calcite from precipitating. On the contrary, calcite might have precipitated during periods of magmatic activity when the $P_{{\rm CO2}}$ (and $\delta^{13}{\rm C}_{{\rm CO2}}$) was higher.

 9.57 ± 0.40 Ra; Tables 1, 2) clearly fingerprint a magmatic outgassing process, as their values are very similar to those of the mantle (–5 \pm 1 % and 8 \pm 1 Ra; Farley and Neroda, 1998; Marty and Zimmermann, 1999). Regional variations in $^3 \text{He/}^4 \text{He}$ across Iceland has been interpreted as a mixing between the MORB-depleted mantle (DMM) and a plume-type mantle (Polak et al., 1976; Torgersen and Jenkins, 1982; Sano et al., 1985; Hilton et al., 1990, 1998; Marty et al., 1991; Poreda et al., 1992; Furi et al., 2010; Stefánsson et al., 2017b). Outgassing from the upper mantle in Krafla gases (9.0–10.4 Ra; Table 1) aligns with such a regional

variation, showing upper mantle-like values in the NVZ (8.4–11.5 Ra; Furi et al., 2010; Saby et al., 2020) and an increase in ³He/⁴He south of the NVZ (16.7–19.2 Ra; Furi et al., 2010) and in the WVZ (9.7–17.4 Ra; inset in Fig. 1a; Furi et al., 2010). Both geothermal fluids and volcanic glasses revealed an increase in ³He/⁴He towards the north within the NVZ (Furi et al., 2010; Harðardóttir et al., 2018; Saby et al., 2020; Ranta et al., 2023). The highest plume-like values (>20 Ra), reflecting a contribution from the deep mantle, are found far from the neovolcanic zone in the South Iceland Seismic Zone (SISZ), a transform fault system separating the EVZ and the WVZ, and in Vestfirðir (NW Iceland; Furi et al., 2010).

Geothermal well and fumarole fluids show almost identical $\delta^{13}C_{CO2}$, (–4.2 \pm 0.4 % and –4.4 \pm 0.3 %, respectively; Table 1, 2; Fig. 11) and are very similar to the $\delta^{13}C_{\text{CO2}}$ of the diffusive degassing of CO_2 from Krafla soils (-4.7 ± 1.1 %; Bini et al., 2024), implying no significant C isotope modification from the productive aquifer depths (down to approximately 1.5 km b.s.l.) up to the surface. This $\delta^{13}C_{CO2}$ of the geothermal fluids is very similar to the canonical value of the upper mantle (-5 ± 1 %; Marty and Zimmermann, 1999) but it is lower than the value estimated for the Icelandic mantle (-2.5 ± 1.1 %; Barry et al., 2014), which is instead recorded in the calcite samples recovered down to approximately 1.5 km b.s.l. during geothermal well drilling ($-2.8 \pm$ 1.2 %; Bini et al., 2024; inset in Fig. 11). This discrepancy between the δ¹³C_{CO2} of the current geothermal fluids and calcites suggests that calcite precipitation occurred in the past, possibly during periods of magmatic activity, such as the Krafla Fires. In fact, magmatic outgassing progressively fractionates C isotopes towards lighter $\delta^{13}\text{C}$ in both the exsolved gas phase and residual melt (Halloway and Blank, 1994). This process has recently been observed during the Litli Hrútur eruption in Reykjanes (Iceland) in 2023, where the gas plume showed more positive $\delta^{13} C_{\text{CO2}}$ values during the eruptive phase, and shifted towards more negative values after the eruption (Fischer et al., 2024). The more positive $\delta^{13}\text{C}$ recorded by calcites may imply CO_2 degassing from primitive magmas during eruptive periods, whereas the lower $\delta^{13}C_{CO2}$ of the fluids currently discharged at Krafla may reflect a degassed magma (a posteruptive period). It is worth noting that during the last eruptive activity of the Krafla Fires (1976-1978) the CO₂ concentration of the KJ-7 well discharge increased up to ~22,500 µmol mol⁻¹ and then decreased to ~800 µmol mol⁻¹ in 1984 (Ármannsson et al., 1989). Such an increase in the P_{CO2} would favor calcite precipitation by destabilizing mineral buffers, such as that including clinozoisite-calcite-quartz-prehnite, consuming prehnite to produce calcite as well as clinozoisite and quartz (Table S2; Fig. 4a). On the contrary, the lower P_{CO2} of the current wet-steam discharged from Krafla seems to prevent calcite precipitation.

6. Conclusions

In this work, we presented an extensive dataset of chemical and isotopic analyses of fumarole vapors and wet-steam well discharges to reconstruct the primary aquifer temperatures and fluid sources sustaining the Krafla geothermal system. Gas equilibrium in the H₂O-H2-CO2-CO-CH4 system for wet-steam well discharges (after Giggenbach, 1980 and Chiodini and Marini, 1998) provides temperatures closer to the measured aquifer temperatures than water geothermometers and the CH₄.CO₂ isotope exchange and sheds light on secondary processes occurring during the exploitation of the geothermal resource. The estimated temperatures (272-320 °C) closely matched those of the main productive zones of geothermal wells and revealed a deep aquifer with a high fraction of equilibrium vapor as the principal source of the steam used for electricity production at Krafla. Fumarole vapors are also sourced from the deep aquifer, as revealed by their equilibrium temperatures (282–322 $^{\circ}\text{C}\text{)},$ although steam condensation and mixing with shallow groundwaters appear to affect their composition. This gas-equilibrium technique is particularly valuable for geothermal fields discharging excess-enthalpy fluids, where scaling or minimal liquid discharge hinders the application of solute geothermometry. In the case

of Krafla, both ${\rm SiO_2}$ and Na-K geothermometers record temperatures lower than those measured in the deep aquifer, suggesting contribution of liquids from less important, cooler production zones at shallower depths. Our findings demonstrate that the ${\rm H_2O\text{-}H_2\text{-}CO_2\text{-}CO\text{-}CH_4}$ gas-system can be employed not only to reconstruct the aquifer temperatures but also to monitor the geothermal production. Significant addition of water was observed in well discharges that experienced a notable decline in the discharge enthalpy in the last 20 years, approaching liquid-like enthalpy. This correlation suggests the effect of geothermal liquid reinjection or downflow from a shallower liquid aquifer interposed between the surface and the deeper two-phase aquifer in Leirbotnar and Vesturhlíðar subfields.

The isotopes of H₂O, CO₂, N₂, Ar, and He provided insights into the sources of the geothermal fluids and the activity of the geothermal system. While H₂O isotopes reflect meteoric and reinjection fluids, the δ^{13} C of CO₂ and 3 He/ 4 He ratios indicate a clear mantle origin. However, the lower $\delta^{13}C_{CO2}$ and P_{CO2} of the current gas emission relative to the Icelandic Mantle δ^{13} C-signature recorded in calcites (Bini et al., 2024), suggest outgassing from a degassed magma, inhibiting calcite precipitation. On the contrary, calcite precipitation appears to have been favored during eruptive periods, when higher P_{CO2} and $\delta^{13}C_{CO2}$ were observed. Ar and N isotopes of excess-enthalpy well-discharges show the addition of vapor rich in Ar and N₂, but depleted in 40 Ar/ 36 Ar and δ^{15} N – below the ASW values. This enrichment in lighter isotopes may reflect fractionation of an ASW-like reservoir liquid due to processes observed in other geothermal system worldwide, such as diffusive transport fractionation (Marty, 1984; Bekaert et al., 2023), repeated boiling (Labidi et al., 2020), and reinjection. These findings emphasize the importance of carefully interpreting noble gas signatures in geothermal fluids for tracing their origin, especially to avoid attributing negative $\delta^{15}N$ values solely to magmatic degassing.

CRediT authorship contribution statement

Giulio Bini: Writing – review & editing, Writing – original draft, Visualization, Methodology, Investigation, Formal analysis, Data curation, Conceptualization. Matteo Lelli: Investigation. Stefano Caliro: Writing – review & editing, Resources, Investigation. Tullio Ricci: Writing – review & editing, Investigation. Anette K. Mortensen: Writing – review & editing, Resources. Ásgerður K. Sigurðardóttir: Writing – review & editing, Resources. Alessandro Santi: Investigation. Antonio Costa: Writing – review & editing, Funding acquisition.

Declaration of competing interest

The authors declare that they have no known competing financial interests or personal relationships that could have appeared to influence the work reported in this paper.

Acknowledgments

We would like to express our sincere gratitude to Luigi Marini (STEAM Srl, Pisa, Italy) for his invaluable contributions to this study. His ideas, along with his work in conceptualization, methodology, formal analysis, visualization, and writing, were pivotal to the development of this paper, which would not have been possible without his insight and expertise. We are also deeply grateful to Giovanni Chiodini (INGV-OV, Napoli, Italy) for his valuable suggestions and insightful discussions, which were instrumental in shaping this manuscript. This study has received funding from the European Union's Horizon 2020 research and innovation program under grant agreement No 858092 (IMPROVE project), from the MIUR, project no PRIN2017–2017LMNLAW "Connect4Carbon", and from the EU-Next Generation EU-PRIN 2022–2022WE2JY9 "SCHOTTA" project. Helgi A. Alfredsson, Teitur Hinrichsen, and Julia Reimer from Landsvirkjun are thanked for the support during well fluid sampling and chemical analyses of liquid

phases at Krafla. We would like to thank Landsvirkjun for granting permission to publish the data on the concentrations of Krafla geothermal liquids. Manfredi Longo (INGV, Palermo, Italy) is thanked for He isotope analyses. Finally, we thank three anonymous reviewers for their constructive comments.

Supplementary materials

Supplementary material associated with this article can be found, in the online version, at doi:10.1016/j.geothermics.2025.103322.

Data availability

Data is available in the manuscript and in the Supplementary Material

References

- Ármannsson, H., Benjamínsson, J., Jeffrey, A.W.A., 1989. Gas changes in the Krafla geothermal system, Iceland. Chem. Geol. 76, 175–196.
- Árnason, K., 2020. New conceptual model for the magma-hydrothermal-tectonic system of Krafla, NE Iceland. Geosciences 10, 34.
- Arnórsson, S., 1970. Underground temperatures in hydrothermal areas in Iceland as deduced from the silica content of the thermal water. Geothermics. 2, 536–541.
- Arnórsson, S., Gunnlaugsson, E., Svavarsson, H., 1983. The chemistry of geothermal waters in Iceland III. Chemical geothermometry in geothermal investigations. Geochim. Cosmochim. Acta 47, 567–577.
- Arnórsson, S., Gunnlaugsson, E., 1985. New gas geothermometers for geothermal exploration— calibration and application. Geochim. Cosmochim. Acta 49, 1307–1325.
- Arnórsson, S., Björnsson, S., Muna, Z.W., Bwire-Ojiambo, S., 1990. The use of gas chemistry to evaluate boiling processes and initial steam fractions in geothermal reservoirs with an example from the Olkaria field, Kenya. Geothermics. 19 (6), 497–514.
- Arnórsson, S., Stefánsson, A., 2005. Wet-steam well discharges. II. Assessment of aquifer fluid compositions. In: Proceedings World Geothermal Congress. Antalya, Turkey, 24-29 April 2005.
- Arnórsson, Ś., Stefánsson, A., Bjarnason, J.O., 2007. Fluid-fluid interactions in geothermal systems. Rev. Mineral. Geochem. 65 (1), 259–312.
- Arnórsson, S., Angcoy, E., Bjarnason, J.Ö., Giroud, N., Gunnarsson, I., Kaasalainen, H., Karingithi, C., Stefánsson, A., 2010. Gas chemistry of volcanic geothermal systems. In: Proceedings World Geothermal Congress, Bali, Indonesia, pp. 25–29.
- Barry, P.H., Hilton, D.R., Füri, E., Halldórsson, S.A., Grönvold, K., 2014. Carbon isotope and abundance systematics of Icelandic geothermal gases, fluids and subglacial basalts with implications for mantle plume-related CO₂ fluxes. Geochim. Cosmochim. Acta 134, 74–99.
- Beaudry, P., Stefánsson, A., Fiebig, J., Rhim, J.H., Ono, S., 2021. High temperature generation and equilibration of methane in terrestrial geothermal systems: evidence from clumped isotopologues. Geochim. Cosmochim. Acta 309, 209–234.
- Bekaert, D.V., Barry, P.H., Broadley, M.W., Byrne, D.J., Marty, B., Ramírez, C.J., de Moor, M.J., Rodriguez, A., Hudak, M.R., Subhas, A.V., Halldórsson, S.A., Stefánsson, A., Caracausi, A., Lloyd, K.G., Giovannelli, D., Seltzer, A.M., 2023. Ultrahigh-precision noble gas isotope analyses reveal pervasive subsurface fractionation in hydrothermal systems. Sci. Adv. 9 (15), eadg2566.
- Bertrami, R., Cioni, R., Corazza, E., D'Amore, F., Marini, L., 1985. Carbon monoxide in geothermal gases. Reservoir temperature calculation at Larderello (Italy). Geotherm. Res. Council Trans. 9, 299–303.
- Bini, G., Chiodini, G., Caliro, S., Tassi, F., Vaselli, O., Rizzo, A.L., Mollo, S., Vougioukalakis, G.E., Bachmann, O., 2022. Nitrogen, helium, and argon reveal the magmatic signature of fumarole gases and episodes of outgassing from upper-crustal magma reservoirs: the case of the Nisyros caldera (Aegean Arc, Greece). Geochim. Cosmochim. Acta 335, 68–84.
- Bini, G., Chiodini, G., Ricci, T., Sciarra, A., Caliro, S., Mortensen, A.K., Martini, M., Mitchell, A., Santi, A., Costa, A., 2024. Soil ${\rm CO}_2$ emission and stable isotopes ($\delta^{13}{\rm C}$, $\delta^{18}{\rm O}$) of ${\rm CO}_2$ and calcites reveal the fluid origin and thermal energy in the supercritical geothermal system of Krafla, Iceland. J. Volcanol. Geothermal Res. 447, 108032.
- Bird, D.K., Norton, D.L., 1981. Theoretical prediction of phase relations among aqueous solutions and minerals: salton Sea geothermal system. Geochim. Cosmochim. Acta 45, 1479–1494.
- Bjarnason, J.Ö., 2010. The Chemical Speciation Program WATCH, Version 2.4. ÍSOR Iceland Geosurvey, Reykjavík, Iceland (Accessible at. https://en.isor.is/software/.
- Caliro, S., Viveiros, F., Chiodini, G., Ferreira, T., 2015. Gas geochemistry of hydrothermal fluids of the S. Miguel and Terceira Islands. Azores. Geochim. Cosmochim. Acta 168, 43–57.
- Chase, M.W., 1998. NIST-JANAF thermochemical tables. J. Phys. Chem. Reference Data 1529-1564.
- Chiodini, G., Cioni, R., 1989. Gas geobarometry for hydrothermal systems and its application to some Italian geothermal areas. Appl. Geochem. 4 (5), 465–472.
- Chiodini, G., Cioni, R., Leonis, C., Marini, L., Raco, B., 1993. Fluid geochemistry of Nisyros island, Dodecanese, Greece. J. Volcanol. Geothermal Res. 56, 95–112.

- Chiodini, G., Marini, L., 1998. Hydrothermal gas equilibria: the H₂O-H₂-CO₂-CO-CH₄ system. Geochim. Cosmochim. Acta 62 (15), 2673–2687.
- Chiodini, G., Marini, L., Russo, M., 2001. Geochemical evidence for the existence of hightemperature hydrothermal brines at Vesuvio volcano, Italy. Geochim. Cosmochim. Acta 65 (13), 2129–2147.
- Cioni, R., Corazza, E., 1981. Medium-temperature fumarolic gas sampling. Bull. Volcanologique 44, 23–29.
- Cioni, R., Marini, L., 2020. A thermodynamic approach to water geothermometry. Springer Geochemistry Series. Springer Nature, Cham, Switzerland.
- D'Amore, F., Panichi, C., 1980. Evaluation of deep temperatures of hydrothermal systems by a new gas geothermometer. Geochim. Cosmochim. Acta 44 (3), 549–556.
- Darling, W.G., Ármannsson, H., 1989. Stable isotopic aspects of fluid flow in the Krafla, Námafjall and Theistareykir geothermal systems of northeast Iceland. Chem. Geol. 76, 197–213.
- Einarsson, P., 1991. Earthquakes and present-day tectonism in Iceland. Tectonophysics. 189, 261–279.
- Einarsson, P., 2008. Plate boundaries, rifts and transforms in Iceland. J.kull J. 58, 35–58. Elders, W.A., Friðleifsson, G.Ó., Zierenberg, R.A., Pope, E.C., Mortensen, A.K., Guðmundsson, Á., Lowenstern, J.B., Marks, N.E., Owens, L., Bird, D.K., Reed, M., Olsen, N.J., Schiffman, P., 2011. Origin of a rhyolite that intruded a geothermal well while drilling at the Krafla volcano, Iceland. Geology 39, 231–234.
- Farley, K.A., Neroda, E., 1998. Noble gases in the earth's mantle. Annu Rev. Earth. Planet. Sci. 26 (1), 189–218.
- Fischer, T.P., Mandon, C.L., Nowicki, S., Ericksen, J., Vilches, F.R., Pfeffer, M.A., Aiuppa, A., Bitetto, M., Vitale, A., Fricke, G.M., Stefánsson, A., 2024. CO₂ emissions during the 2023 Litli Hrútur eruption in Reykjanes, Iceland: δ¹³C tracks magma degassing. Bull. Volcanol. 86 (6), 1–10.
- Foong, K.C., 2005. Design concept for a more efficient steam-water separator. In: Proceedings World Geothermal Congress, Antalya, Turkey, 24-29 April 2005.
- Fournier, R.O., 1973. Silica in thermal waters: laboratory and field investigations. Proc.: Hydrogeochem. 1, 122.
- Fournier, R.O., 1979. A revised equation for the Na/K geothermometer. Geotherm. Res. Counc. Trans. 5, 1–16.
- Fournier, R.O., Rowe, J.J., 1962. The solubility of cristobalite along the three-phase curve, gas plus liquid plus cristobalite. Am. Mineralogist: J. Earth Planetary Mater. 47 (7–8), 897–902.
- Fournier, R.O., 1981. Application of water geochemistry to geothermal exploration and reservoir engineering. In: Rybach, L., Muffler, L.J.P. (Eds.), Geothermal systems: Principles and Case Histories. Wiley, New York, pp. 109–143.
- Fournier, R.O., 1991. Water geothermometers applied to geothermal energy. In: D'Amore, F. (Ed.), Application of Geochemistry in Geothermal Reservoir Development. United Nations Institute for Training and Research, New York, pp. 37–69.
- Fournier, R.O., White, D.E., Truesdell, A.H., 1974. Geochemical indicators of subsurface temperature. Part I. Basic assumptions. J. Res. US Geol. Surv. 2 (3), 259–262.
- Fournier, R.O., Potter II, R.W., 1982a. An equation correlating the solubility of quartz in water from 25° to 900°C at pressures up to 10,000 bars. Geochim. Cosmochim. Acta 46, 1969–1973.
- Fournier, R.O., Potter II, R.W., 1982b. A revised and expanded silica (quartz) geothermometer. Geot. Res. Council. Bull. 11, 3–12.
- Füri, E., Hilton, D.R., Halldórsson, S.A., Barry, P.H., Hahm, D., Fischer, T.P., Grönvold, K., 2010. Apparent decoupling of the He and Ne isotope systematics of the Icelandic mantle: the role of He depletion, melt mixing, degassing fractionation and air interaction. Geochim. Cosmochim. Acta 74 (11), 3307–3332.
- Giggenbach, W.F., 1975. A simple method for the collection and analysis of volcanic gas samples. Bull. Volcanol. 39, 132–145.
- Giggenbach, W.F., 1980. Geothermal gas equilibria. Geochim. Cosmochim. Acta 44 (12), 2021–2032.
- Giggenbach, W.F., 1981. Geothermal mineral equilibria. Geochim. Cosmochim. Acta 45 (3), 393–410.
- Giggenbach, W.F., 1988. Geothermal solute equilibria. Derivation of Na-K-Mg-Ca geoindicators. Geochim. Cosmochim. Acta 52 (12), 2749–2765.
- Giggenbach, W.F., 1991. Chemical techniques in geothermal exploration. In: D'Amore, F. (Ed.), Application of Geochemistry in Geothermal Reservoir Development. United Nations Institute for Training and Research, New York, pp. 119–144.
- Giggenbach, W.F., 1992. Isotopic shifts in waters from geothermal and volcanic systems along convergent plate boundaries and their origin. Earth Planet. Sci. Lett. 113 (4), 495–510.
- Giggenbach, W.F., Stewart, M.K., 1982. Processes controlling the isotopic composition of steam and water discharges from steam vents and steam-heated pools in geothermal areas. Geothermics 11 (2), 71–80.
- Giggenbach, W.F., Goguel, R.L., 1989. Collection and analysis of geothermal and volcanic water and gas discharges. Report No. CD 2401. Chemistry Division, DSIR, Petone, New Zealand.
- Giggenbach, W.F., Matsuo, S., 1991. Evaluation of results from second and third IAVCEI Field Workshops on volcanic Gases, Mt Usu, Japan, and White Island, New Zealand. Appl. Geochem. 6, 125–141.
- Glover, R.B., Lovelock, B., Ruaya, J.R., 1981. A Novel Way of Using Gas and Enthalpy.

 New Zealand Geothermal Workshop, Auckland, New Zealand, pp. 163–169.
- Gudmundsson, B.T., Arnórsson, S., 2002. Geochemical monitoring of the Krafla and Námafjall geothermal areas. N-Iceland. Geothermics 31 (2), 195–243.
- Gudmundsson, Á., Mortensen, A.K., 2015. Well locations consideration of purpose, objectives and achievement with emphasis on recent drilling in the Krafla geothermal area. In: Proceedings of the World Geothermal Congress 2015, Melbourne, Australia.

- Gutiérrez-Negrín, L.C., 2024. Evolution of worldwide geothermal power 2020–2023. Geothermal Energy 12 (1), 14.
- Hayba, D.O., Ingebritsen, S.E., 1997. Multiphase groundwater flow near cooling plutons. J. Geophys. Res.: Solid Earth 102 (B6), 12235–12252.
- Hermanská, M., Stefánsson, A., Scott, S., 2019. Supercritical fluids around magmatic intrusions: IDDP-1 at Krafla, Iceland. Geothermics. 78, 101–110.
- $\label{eq:Hilton, D.R., Grönvold, K., O'Nions, R.K., Oxburgh, E.R., 1990. Regional distribution of 3He anomalies in the Icelandic crust. Chem. Geol. 88 (1–2), 53–67.}$
- Hilton, D.R., Grönvold, K., Sveinbjornsdottir, A.E., Hammerschmidt, K., 1998. Helium isotope evidence for off-axis degassing of the Icelandic hotspot. Chem. Geol. 149 (3–4), 173–187.
- Harðardóttir, S., Halldórsson, S.A., Hilton, D.R., 2018. Spatial distribution of helium isotopes in Icelandic geothermal fluids and volcanic materials with implications for location, upwelling and evolution of the Icelandic mantle plume. Chem. Geol. 480, 12–27.
- Hjartardóttir, Á.R., Einarsson, P., Magnúsdóttir, S., Björnsdóttir, T., Brandsdóttir, B., 2016. Fracture systems of the northern volcanic rift zone, Iceland: an onshore part of the mid-Atlantic plate boundary. Geol. Soc., London, Special Publications 420 (1), 297–314.
- Holloway, J.R., Blank, J., 1994. Experimental results applied to C-O-H in natural melts. In: Holloway, J.R. (Ed.), Volatiles in Magmas. Reviews in Mineralogy. Mineral Soc, America, Fredericksburg, VA, pp. 187–230.
- Johnson, J.W., Oelkers, E.H., Helgeson, H.C., 1992. SUPCRT92: a software package for calculating the standard molal thermodynamic properties of minerals, gases, aqueous species, and reactions from 1 to 5000 bar and 0 to 1000 C. Comput. Geosci. 18 (7), 899–947.
- Labidi, J., Barry, P.H., Bekaert, D.V., Broadley, M.W., Marty, B., Giunta, T., Warr, O., Sherwood, L.B., Fischer, T.P., Avice, G., Caracausi, A., Ballentine, C.J., Halldórsson, S.A., Stefánsson, A., Kurz, M.D., Kohl, I.E., Young, E.D., 2020. Hydrothermal ¹⁵N¹⁵N abundances constrain the origins of mantle nitrogen. Nature 580, 367–371.
- Lee, J.-Y., Marti, K., Severinghaus, J.P., Kawamura, K., Yoo, H.-S., Lee, J.B., Kim, J.S., 2006. A redetermination of the isotopic abundances of atmospheric Ar. Geochim. Cosmochim. Acta 70, 4507–4512.
- Lee, H., Sharp, Z.D., Fischer, T.P., 2015. Kinetic nitrogen isotope fractionation between air and dissolved N_2 in water: implications for hydrothermal systems. Geochem. J. 49 (5), 571–573.
- Lund, J.W., Toth, A.N., 2021. Direct utilization of geothermal energy 2020 worldwide review. Geothermics. 90, 101915.
- Marini, L., Fiebig, J., 2005. Fluid geochemistry of the magmatic-hydrothermal system of Nisyros (Greece). In: Hunziker, J.C., Marini, L. (Eds.), The Geology, Geochemistry and Evolution of Nisyros Volcano (Greece). Implications for the Volcanic Hazards. Memoires de Géologie, Lausanne, pp. 121–163.
 Marini, L., Principe, C., Lelli, M., 2022. The Geoindicators Involving H₂O, CO₂, CO, CH₄
- Marini, L., Principe, C., Lelli, M., 2022. The Geoindicators Involving H₂O, CO₂, CO, CH₄ and H₂, in: The Solfatrara Magmatic-Hydrothermal System: Geochemistry, Geothermometry and Geobarometry of Fumarolic Fluids. Springer International Publishing., Cham, pp. 197–227.
- Marty, B., 1984. On the noble gas, isotopic fractionation in naturally occurring gases. Geochem. J. 18 (3), 157–162.
- Marty, B., Gunnlaugsson, E., Jambon, A., Oskarsson, N., Ozima, M., Pineau, F., Torssander, P., 1991. Gas geochemistry of geothermal fluids, the Hengill area, southwest rift zone of Iceland. Chem. Geol. 91 (3), 207–225.
- Marty, B., Zimmermann, L., 1999. Volatiles (He, C, N, Ar) in mid-ocean ridge basalts: assessment of shallow-level fractionation and characterization of source composition. Geochim. Cosmochim. Acta. 63, 3619–3633.
- Marty, B., Dauphas, N., 2003. The nitrogen record of crust–mantle interaction and mantle convection from Archean to present. Earth Planet. Sci. Lett. 206, 397–410.
- Mishima, K., Sumino, H., Yamada, T., Ieki, S., Nagakura, N., Otono, H., Oide, H., 2018. Accurate determination of the absolute ³He/⁴He ratio of a synthesized helium standard gas (helium standard of Japan, HESJ): toward revision of the atmospheric ³He/⁴He ratio. Geochem., Geophys., Geosyst. 19 (10), 3995–4005.
- Montanaro, C., Mortensen, A.K., Weisenberger, T.B., Dingwell, D.B., Scheu, B., 2021. Stratigraphic reconstruction of the Viti breccia at Krafla volcano (Iceland): insights into pre-eruptive conditions priming explosive eruptions in geothermal areas. Bull. Volcanol. 83, 81.
- Mortensen, A.K., Grönvold, K., Gudmundsson, Á., Steingrímsson, B., Egilson, F., 2010. Quenched silicic glass from well KJ-39 in Krafla, North-Eastern Iceland. In: Proceedings World Geothermal Congress 2010, Bali, Indonesia.
- Mortensen, A.K., Gudmundsson, Á., Steingrímsson, B., Sigmundsson, F., Axelsson, G., Ármannsson, H., Hauksson, T., 2015. The Krafla geothermal system: Research summary and Conceptual Model Revision (Tech. Rep. No. LV-2015-098). Landsvirkiun.
- Nagao, K., Takaoka, N., Matsubayashi, O., 1979. Isotopic anomalies of rare gases in the Nigorikawa geothermal area, Hokkaido, Japan. Earth Planet. Sci. Lett. 44 (1), 82–90.
- Nagao, K., Takaoka, N., Matsubayashi, O., 1981. Rare gas isotopic compositions in natural gases of Japan. Earth Planet. Sci. Lett. 53 (2), 175–188.
- Nicholson, H., Condomines, M., Fitton, J.G., Fallick, A.E., Gr Nvold, K., Rogers, G., 1991. Geochemical and isotopic evidence for crustal assimilation beneath Krafla, Iceland. J. Petrol. 32, 1005–1020.
- Óskarsson, F., Inguaggiato, S., Fridriksson, Th., Caliro, S., 2015. Gas isotope characterisation of the Reykjanes geothermal field, Iceland. In: Proc. World Geotherm. Cong. 2015, Melbourne, Australia.

Ozima, M., Podosek, F.A., 2002. Noble Gas Geochemistry. Cambridge University Press. Panichi, C., 2004. Geochemical impact of re-injecting geothermal waste waters: example, Larderello, Italy. In: Geological Society, 236. Special Publications, London, pp. 337–354.

- Polak, G., Kononov, I., Tolstikhin, I., Mamyrin, B.A., Khabarin, L.V., 1976. The helium isotopes in thermal fluids. In thermal and chemical problems of thermal waters. Int. Assoc. Hydrogeol. Sci. 119, 17–33.
- Pope, E.C., Bird, D.K., Arnórsson, S., 2013. Evolution of low-¹⁸O Icelandic crust. Earth . Planet. Sci. Lett. 374, 47–59.
- Pope, E.C., Bird, D.K., Arnórsson, S., Giroud, N., 2016. Hydrogeology of the Krafla geothermal system, northeast Iceland. Geofluids 16, 175–197.
- Poreda, R.J., Craig, H., Arnorsson, S., Welhan, J.A., 1992. Helium isotopes in Icelandic geothermal systems: I. ³He, gas chemistry, and ¹³C relations. Geochim. Cosmochim. Acta 56 (12), 4221–4228.
- Ranta, E., Halldórsson, S.A., Barry, P.H., Ono, S., Robin, J.G., Kleine, B.I., Ricci, A., Fiebig, J., Sveinbjörnsdóttir, Á.E., Stefánsson, A., 2023. Deep magma degassing and volatile fluxes through volcanic hydrothermal systems: insights from the Askja and Kverkfjöll volcanoes, Iceland. J. Volcanol. Geothermal Res. 436, 107776.
- Rizzo, A.L., Caracausi, A., Chavagnac, V., Nomikou, P., Polymenakou, P., Mandalakis, M., Kotoulas, G., Magoulas, A., Castillo, A., Lampridou, D., 2016. Kolumbo submarine volcano (Greece): an active window into the Aegean subduction system. Sci. Rep. 6, 28013.
- Rooyakkers, S.M., Stix, J., Berlo, K., Barker, S.J., 2020. Emplacement of unusual rhyolitic to basaltic ignimbrites during collapse of a basalt-dominated caldera: the Halarauður eruption, Krafla (Iceland). Bulletin 132 (9–10), 1881–1902.
- Rooyakkers, S.M., Stix, J., Berlo, K., Petrelli, M., Hampton, R.L., Barker, S.J., Morgavi, D., 2021. The origin of rhyolitic magmas at Krafla Central Volcano (Iceland). J. Petrol. 62, egab064.
- Saby, M., Pinti, D.L., van Hinsberg, V., Gautason, B., Sigurðardóttir, Á., Castro, C., Hall, C., Óskarsson, F., Rocher, O., Hélie, J.F., Méjean, P., 2020. Sources and transport of fluid and heat at the newly-developed Theistareykir Geothermal Field, Iceland. J. Volcanol. Geothermal Res. 405, 107062.
- Sano, Y., Urabe, A., Wakita, H., Chiba, H., Sakai, H., 1985. Chemical and isotopic compositions of gases in geothermal fluids in Iceland. Geochem. J. 19 (3), 135–148.
- Sæmundsson, K., 2008. Krafla Geological map. 1:25.000. Landsvirkjun and ÍSOR.
- Sano, Y., Takahata, N., Nishio, Y., Fischer, T.P., Williams, S.N., 2001. Volcanic flux of nitrogen from the Earth. Chem. Geol. 171, 263–271.
- Sepúlveda, F., Lahsen, A., Powell, T., 2007. Gas geochemistry of the Cordón Caulle geothermal system, Southern Chile. Geothermics. 36 (5), 389–420.
- Scott, S., Gunnarsson, I., Arnórsson, S., Stefánsson, A., 2014. Gas chemistry, boiling and phase segregation in a geothermal system, Hellisheidi, Iceland. Geochim. et Cosmochim. Acta 124, 170–189.
- Scott, S.W., O'Sullivan, J.P., Maclaren, O.J., Nicholson, R., Covell, C., Newson, J., Guðjónsdóttir, M.S., 2022. Bayesian calibration of a natural State geothermal reservoir model, Krafla, North Iceland. Water. Resour. Res. 58.
- Stefánsson, A., 2014. Geochemical Assessment of the Utilization of IDDP#1, Krafla (Tech. Rep. No. LV-2014-007). Landsvirkjun.
- Stefánsson, A., 2017. Gas chemistry of Icelandic thermal fluids. J. Volcanol. Geothermal Res. 346, 81–94.
- Stefánsson, A., Arnórsson, S., 2002. Gas pressures and redox reactions in geothermal fluids in Iceland. Chem. Geol. 190 (1–4), 251–271.
- Stefánsson, A., Hilton, D.R., Sveinbjörnsdóttir, Á.E., Torssander, P., Heinemeier, J., Barnes, J.D., Ono, S., Halldórsson, S.A., Fiebif, J., Arnórsson, S., 2017. Isotope systematics of Icelandic thermal fluids. J. Volcanol. Geothermal Res. 337, 146–164.
- Stefánsson, A., Ricci, A., Garnett, M., Gunnarsson-Robin, J., Kleine-Marshall, B.I., Scott, S.W., Lelli, M., Dantas Cardoso, C., Pik, R., Santinelli, C., Ono, S., Barry, P.H., Broadley, M.W., Byrne, D., Halldórsson, S.A., Fiebig, J., 2024. Isotopic and kinetic constraints on methane origins in Icelandic hydrothermal fluids. Geochim. Cosmochim. Acta 373, 84–97.
- Stefánsson, V., 1981. The Krafla geothermal field, northeast Iceland. In: Rybach, L., Muffler, L.J.P. (Eds.), Geothermal systems: Principles and Case Studies. Wiley-Interscience, pp. 273–293.
- Sveinbjörnsdóttir, Á.E., 1992. Composition of geothermal minerals from saline and dilute fluids —Krafla and Reykjanes, Iceland. Lithos. 27, 301–315.
- Sveinbjornsdottir, A.E., Coleman, M.L., Yardley, B.W.D., 1986. Origin and history of hydrothermal fluids of the Reykjanes and Krafla geothermal fields, Iceland: a stable isotope study. Contr. Mineral. Petrol. 94, 99–109.
- Torgersen, T., Jenkins, W.J., 1982. Helium isotopes in geothermal systems: iceland, The Geysers, Raft River and Steamboat Springs. Geochim. Cosmochim. Acta 46 (5), 739-748
- Troch, J., Ellis, B.S., Harris, C., Bachmann, O., Bindeman, I.N., 2020. Low-δ¹⁸O silicic magmas on Earth: a review. Earth Sci. Rev. 208, 103299.
- Truesdell, A.H., White, D.E., 1973. Production of superheated steam from vapor-dominated geothermal reservoirs. Geothermics. 2 (3–4), 154–173.
- Wagner, W., Pruss, A., 2002. The IAPWS formulation 1995 for the thermodynamic properties of ordinary water substance for general and scientific use. J. Phys. Chem. Ref. Data 31 (2), 387–535.
- Weisenberger, T.B., Axelsson, G., Arnaldsson, A., Blischke, A., Óskarsson, F., Ármannsson, H., Blanck, H., et al., 2015. Revision of the Conceptual Model of the Krafla geothermal System (Tech. Rep. No. LV-2015-040). Landsvirkjun.